

Measuring turbulent motion in planet-forming disks with ALMA: A detection around DM Tau and non-detections around MWC 480 and V4046 Sgr

KEVIN FLAHERTY,¹ A. MEREDITH HUGHES,² JACOB B. SIMON,^{3,4,5} CHUNHUA QI,⁶ XUE-NING BAI,^{7,8} ALYSSA BULATEK,⁹
SEAN M. ANDREWS,⁶ DAVID J. WILNER,⁶ AND ÁGNES KÓSPÁL^{10,11,12}

¹*Department of Astronomy and Department of Physics
Williams College, Williamstown, MA 01267 USA*

²*Van Vleck Observatory, Astronomy Department, Wesleyan University
96 Foss Hill Drive
Middletown, CT 06459, USA*

³*Department of Physics and Astronomy, Iowa State University, Ames, IA, 50010, USA*

⁴*Department of Space Studies, Southwest Research Institute
Boulder, CO 80302*

⁵*JILA, University of Colorado and NIST
440 UCB, Boulder, CO 80309*

⁶*Harvard-Smithsonian Center for Astrophysics
60 Garden St
Cambridge, MA 02138*

⁷*Institute for Advanced Study
Tsinghua University
Beijing 100084, China*

⁸*Tsinghua Center for Astrophysics
Tsinghua University
Beijing 100084, China*

⁹*Department of Physics & Astronomy
Macalester College
1600 Grand Avenue, Saint Paul, MN 55105*

¹⁰*Konkoly Observatory, Research Centre for Astronomy and Earth Sciences,
Konkoly-Thege Meklós út 15-17, 1121 Budapest, Hungary*

¹¹*Max Planck Institute for Astronomy, Königstuhl 17, D-69117 Heidelberg, Germany*

¹²*ELTE Eötvös Loránd University, Institute of Physics, Pázmány Péter sétány 1/A, 1117 Budapest, Hungary*

ABSTRACT

Turbulence is a crucial factor in many models of planet formation, but it has only been directly constrained among a small number of planet forming disks. Building on the upper limits on turbulence placed in disks around HD 163296 and TW Hya, we present ALMA CO J=2-1 line observations at $\sim 0''.3$ (20-50 au) resolution and 80 ms^{-1} channel spacing of the disks around DM Tau, MWC 480, and V4046 Sgr. Using parametric models of disk structure, we robustly detect non-thermal gas motions around DM Tau of between $0.25 c_s$ and $0.33 c_s$, with the range dominated by systematic effects, making this one of the only systems with directly measured non-zero turbulence. Using the same methodology, we place stringent upper limits on the non-thermal gas motion around MWC 480 ($< 0.08 c_s$) and V4046 Sgr ($< 0.12 c_s$). The preponderance of upper limits in this small sample, and the modest turbulence levels consistent with dust studies, suggest that weak turbulence ($\alpha \lesssim 10^{-3}$) may be a common, albeit not universal, feature of planet-forming disks. We explore the particular physical conditions around DM Tau that could lead this system to be more turbulent than the others.

1. INTRODUCTION

Understanding the connection between disks around young stars and the planets formed within these environments requires knowledge about a wide range of

physical processes, as well as how these processes vary between different stellar systems. One of the key disk properties is the non-thermal, non-Keplerian turbulent motion, which theoretically influences a range of processes ranging from the growth of grains from micron-sizes up to planets (e.g. Ormel & Cuzzi 2007; Birnstiel et al. 2010) and the orbital evolution of fully-formed planets (e.g. Nelson & Papaloizou 2004; Paardekooper et al. 2011; Fung et al. 2014) to the chemical (Semenov & Wiebe 2011; Furuya & Aikawa 2014; Xu et al. 2017) and angular momentum (e.g. Lynden-Bell & Pringle 1974) evolution of the disk.

Efforts to broadly characterize the turbulence among a large sample of young stellar objects have relied on indirect techniques. Assuming that a planet-forming disk evolves through viscous processes, in which angular momentum is transported outwards while mass is transported inwards, leads to a predicted connection between accretion rate, disk mass, disk radius, and time (Hartmann et al. 1998) that can be used to constrain turbulence. In the context of an α -disk model of viscosity (Shakura & Sunyaev 1973), in which the viscosity (ν) is equal to the product of α , the local sound speed (c_s), and the gas pressure scale height (H), a number of studies have examined various predictions of viscous evolution using samples of ~ 30 -50 sources (Stepinski 1998; Mulders, et al. 2017; Lodato, et al. 2017; Rafikov 2017; Ansdell et al. 2018; Najita & Bergin 2018) and have found a wide range of α values (10^{-4} - 0.1). Mulders & Dominik (2012) rely on the connection between turbulence and the settling of dust grains (e.g. Youdin & Lithwick 2007), and use the average spectral energy distributions of Herbig stars, T-Tauri stars, and brown dwarfs to find that $\alpha \sim 10^{-4}$ best reproduces the average emission profile. High resolution continuum imaging of dust structures also provides constraints on non-thermal motion through the sharpness and morphology of both dark gaps and bright rings (e.g. Pinte, et al. 2016; Huang et al. 2018; Dullemond et al. 2018).

Gas motion provides a more direct measure of the turbulence, but observational constraints are limited to small samples. Hughes et al. (2011) studied the disks around HD 163296 and TW Hya, while Guilloteau et al. (2012) studied the disk around DM Tau. In the ALMA era, TW Hya and HD 163296 have been revisited (Flaherty et al. 2015; Teague et al. 2016; Flaherty et al. 2017; Flaherty, et al. 2018; Teague et al. 2018a), finding upper limits on the turbulence of $\lesssim 5$ -10% of the local sound speed for gas at distances of ~ 30 au and larger from the central star. Near-infrared observations, more sensitive to gas within a few au of the central star, have found evidence of non-thermal broadening components compa-

rable to the local sound speed among samples of similar sizes (Carr et al. 2004; Najita et al. 2009; Doppmann et al. 2011; Ilee et al. 2014).

Here we build on our previous efforts to measure turbulence directly from ALMA observations of molecular gas emission lines to include the disks around DM Tau, MWC 480, and V4046 Sgr. While still representing a modest sample, these sources were chosen to cover a range of accretion rates, X-ray luminosities, and far-ultraviolet (FUV) luminosities. This parameter space is particularly relevant for the magneto-rotational instability (Balbus & Hawley 1998). The MRI relies on the coupling between gas and magnetic field to destabilize a rotating disk to generate the correlated turbulent fluctuations that can transport angular momentum and drive accretion through the disk. The outcome of the MRI, especially the level of turbulence, is sensitive to the level of disk ionization (e.g. Simon et al. 2018). Therefore, observationally establishing a relation between turbulence and other disk parameters offers important physical insight into the microphysical processes governing disk evolution.

In section 2 we present the ALMA observations of these three systems, and in section 3 we discuss our framework for modeling the CO emission. We present our finding of weak turbulence around MWC 480 and V4046 Sgr, and non-zero turbulence around DM Tau in section 4, while in section 5 we examine the evidence that weak turbulence may be common among planet-forming disks, as well as the physical conditions that influence the difference in the measured level of turbulence between DM Tau and the other systems.

2. OBSERVATIONS

ALMA band 6 observations of the disks around DM Tau, MWC 480, and V4046 Sgr were taken as part of project 2016.1.00724.S. These observations were split into short and long baseline components in order to capture the full spatial extent of the CO emission (out to $\sim 6''$) at high spatial resolution ($\sim 0''.3$). Observations were taken between December 2016 and July 2017, with baselines ranging from 15 m to 2.6 km (Table 1).

The spectral windows were split between a continuum window centered at 232 GHz, and three windows centered on CO(2-1), ^{13}CO (2-1), and C^{18}O (2-1) respectively. This paper focuses on CO(2-1), while future work will consider the isotopologues. For the spectral lines, the correlator was configured for 960 channels, each 61.035 kHz wide ($\sim 80 \text{ m s}^{-1}$). The standard ALMA reduction scripts were used to produce calibrated visibilities. For each set of observations, two rounds of phase self-calibration and one round of amplitude self-

calibration was performed, based on the high S/N continuum data with the exception of the short-baseline DM Tau observations where the amplitude self-calibration was excluded. The spectra were binned down by a factor of 2 (0.16 km s^{-1}).

Uncertainties in the flux calibration will result in small variations in the flux between the two sets of observations. To remove this effect, we compare the continuum visibilities with baselines $<200 \text{ k}\lambda$ among the two observational epochs. We find that the long baseline observations are 1.06, 1.04, and 0.93 times brighter than the short baselines observations for DM Tau, MWC 480, and V4046 Sgr respectively; the size of the amplitude differences is consistent with that expected from the uncertainty in the ALMA calibration (Butler 2012). These scale factors are applied to the model images before fitting to the long baseline data.

The positional offset of the disk between the two epochs can vary based on e.g. errors in the proper motion correction or errors in the astrometric accuracy of ALMA. We estimate the positional offset between the

short and long baselines observations by fitting an elliptical Gaussian to the continuum observations, and apply a phase offset to each epoch to correct the disk center to the phase center. For MWC 480 the positional offsets are 73 mas, -86 mas in RA and Dec for the short baseline data, and 56 mas, -3 mas for the long baseline data. For the DM Tau disk, the offsets in RA and Dec are 230 mas, 3.6 mas for the short baseline data and 230 mas, -2.2 mas for the long baseline data. No significant offset between the short and long-baseline data was found for V4046 Sgr, although for both data sets the center of the disk was offset by 270 mas in RA and 17 mas in Dec from the phase center, which is included in the models. The observed locations of the disks are consistent with the stellar positions now available in the GAIA DR2 database (Gaia Collaboration et al. 2018). The amplitude differences between the short and long baselines are unaffected by these positional offsets.

Cleaned images were generated by combining the short and long baseline visibilities. Using natural weighting results in $\sim 0''.3\text{-}0''.5$ beam with an rms of 2-4 mJy/beam per 0.16 km s^{-1} wide channel.

Table 1. Observing Summary

Star	Date	Time on source	Baselines	PWV	Calibrators	Phase Center
DM Tau	2016-12-27	10 min	15-459 m	1.5 mm	J0510+1800 (bandpass, phase), J0423-0120 (flux)	04:33:48.732781 +18:10:09.67744
DM Tau	2017-07-05	32 min	21-2647 m	0.61 mm	J0510+1800 (bandpass, phase), J0423-0120 (flux)	04:33:48.733234 +18:10:09.66785
MWC 480	2016-12-27	12 min	15-459 m	1.65 mm	J0510+1800 (bandpass,flux), J0438+3004 (phase)	04:58:46.271217 +29:50:36.52973
MWC 480	2016-10-27	39 min	18-1124 m	0.77 mm	J0510+1800 (bandpass,flux), J0438+3004 (phase)	04:58:46.271713 +29:50:36.53469
V4046 Sgr	2017-04-08	8 min	15-390 m	1.18 mm	Titan (flux), J1924-2914 (bandpass), J1826-2924 (phase)	18:14:10.468875 -32:47:35.43708
V4046 Sgr	2017-05-03	27 min	15-1110 m	0.38 mm	J1924-2914 (flux,bandpass), J1826-2924 (phase)	18:14:10.468886 -32:47:35.44081

3. MODELS

The modeling code used to derive the turbulence has been described previously in Flaherty et al. (2015), Flaherty et al. (2017), and Flaherty, et al. (2018), and is based on earlier work by Rosenfeld et al. (2013a) and Dartois et al. (2003). We summarize the relevant equations below, including the key free parameters and the assumptions made for each source.

The surface density is assumed to follow a power law, with an exponential tail, as expected for a viscously evolving disk (Lynden-Bell & Pringle 1974; Hartmann et al. 1998).

$$\Sigma_{\text{gas}}(r) = \frac{M_{\text{gas}}(2-\gamma)}{2\pi R_c^2} \left(\frac{r}{R_c}\right)^{-\gamma} \exp\left[-\left(\frac{r}{R_c}\right)^{2-\gamma}\right], \quad (1)$$

where M_{gas} , R_c and γ are the gas mass (in M_{\odot}), critical radius (in au) and power law index respectively. The disk extends from R_{in} to 1000 au.

The temperature structure is defined as a power law with radius, with a vertical gradient connecting the cold midplane with the warm atmosphere.

$$T_{\text{mid}} = T_{\text{mid}0} \left(\frac{r}{150 \text{ au}}\right)^q \quad (2)$$

$$T_{\text{atm}} = T_{\text{atm}0} \left(\frac{r}{150 \text{ au}}\right)^q \quad (3)$$

$$T_{\text{gas}}(r, z) = \begin{cases} T_{\text{atm}} + (T_{\text{mid}} - T_{\text{atm}})(\cos \frac{\pi z}{2Z_q})^2 & \text{if } z < Z_q \\ T_{\text{atm}} & \text{if } z \geq Z_q \end{cases} \quad (4)$$

$$Z_q = Z_{q0}(r/150 \text{ au})^{1.3} \quad (5)$$

The parameter Z_q is the height above the midplane at which the gas temperature reaches its maximum value. Once the temperature structure and surface density profile have been specified, the hydrostatic equilibrium cal-

culatation is performed at each radius to derive the gas volume density at each height above the midplane. The velocity field is assumed to be Keplerian, with corrections for the height above the midplane and the pressure support of the gas, as in [Rosenfeld et al. \(2013a\)](#).

The line profile is a Gaussian whose width is set by the thermal and non-thermal motions. We associate the non-thermal term with turbulence (δv_{turb}) although we consider other sources of non-Keplerian, non-thermal motion in section 4.1.1. We focus on cases in which the non-thermal term is proportional to the local isothermal sound speed:

$$\Delta V = \sqrt{(2k_B T(r, z)/m_{\text{CO}})(1 + \delta v_{\text{turb}}^2)}. \quad (6)$$

This parameterization is physically motivated by numerical simulations that predict that the turbulence scales with the local sound speed (e.g. [Shi & Chiang 2014](#); [Simon, et al. 2015](#); [Flock, et al. 2017](#)).

One important component in fitting the CO observations is the midplane temperature. As demonstrated in [Flaherty, et al. \(2018\)](#), an overestimate of the midplane temperature can lead to an underestimate of the turbulence. The data themselves do not provide strong constraints on the midplane temperature; C¹⁸O(2-1) has a strong degeneracy between T_{mid} and the CO abundance, while CO(2-1), unlike other systems (e.g. [Rosenfeld et al. 2013a](#); [Pinte et al. 2018a](#); [Dullemond et al. 2019](#)), does not have enough sight lines at low optical depth that reach to the midplane.

For DM Tau, the value of $T_{\text{mid}0}$ is chosen such that CO freeze-out at the midplane ($T_{\text{mid}}=19$ K) occurs at 70 au, as predicted by the chemical models of [Loomis et al. \(2015\)](#). To preserve the location of CO freeze-out while the temperature structure, through the parameter q , is varied during the model fitting, the exact value of the $T_{\text{mid}0}$ parameter is defined based on the value of q (i.e. $T_{\text{mid}0}=19(70/150)^{-q}$). For MWC 480, we use the temperature structure derived by [Piétu, et al. \(2007\)](#) based on observations of ¹³CO, which corresponds to $T_{\text{mid}0}=18.8$ K. For the disk around V4046 Sgr, we use a midplane normalization based on a D’Alessio model fitting of the SED, which results in $T_{\text{mid}0}=12$ K (C. Qi, private communication). In addition to these fiducial values, we also consider lower $T_{\text{mid}0}$ values to examine the effect of a different assumed value of the midplane temperature on the turbulence estimates.

In our initial attempts at fitting the CO emission, we found that the models were unable to simultaneously reproduce the emission at radii $\lesssim 200$ au and $\gtrsim 200$ au. This likely reflects complexities in the CO freeze-out/desorption process that are not included in our initial model prescription; we implicitly assume that ther-

mal desorption and photo-dissociation set the CO molecular layer, while recent chemical models have shown that non-thermal desorption effects are important around IM Lup ([Öberg et al. 2015](#)) and TW Hya ([Teague et al. 2017](#)). Similarly, extended cold CO emission has been observed around AS 209 ([Huang et al. 2016](#)), and TW Hya ([Schwarz et al. 2016](#)). To account for non-thermal desorption of CO, we re-introduce CO to the disk in the region between $N_{\text{H}_2} = 1.3$ and $4.8 \times 10^{21} \text{ cm}^{-2}$ when $T_{\text{gas}} < 20$ K, as described in Appendix A.

In our fiducial models we allow $T_{\text{atm}0}$, q , R_c , i , δv_{turb} , and R_{in} to vary, along with the systemic velocity of the disk (v_{sys}). Table 2 lists the fixed parameters for each source. All distances are based on GAIA DR2 parallax measurements ([Gaia Collaboration et al. 2018](#); [Lindgren et al. 2018](#)). The position angle of the disk is determined based on initial fitting of the system (PA=154.8°, 147.8°, 75.65° for DM Tau, MWC 480, and V4046 Sgr respectively), and was kept fixed due to its independence from the other model parameters, while γ is always fixed at 1. For the disk around V4046 Sgr, we use the sum of the masses of the two stars to set the Keplerian motion of the disk. The sign on the inclination is adjusted so as to minimize asymmetric residuals (Appendix B). Using GAIA DR2 distances [Simon et al. \(2019\)](#) derive stellar masses for MWC 480 and DM Tau of $2.11 \pm 0.01 M_{\odot}$ and $0.55 \pm 0.02 M_{\odot}$ respectively. Utilizing these updated masses will most strongly affect the derived inclination (e.g. [Czekala et al. 2016](#)) while their affect on turbulence is likely to be small, especially for DM Tau, and will be investigated in more detail in future work.

The posterior distributions for each parameter are estimated using the MCMC routine EMCEE ([Foreman-Mackey et al. 2013](#)), based on the Affine-Invariant algorithm originally proposed in [Goodman & Weare \(2010\)](#). The uncertainties in the data are estimated based on the calculated dispersion among baselines of similar distances in line-free channels. Typical MCMC chains consist of 80 walkers and 800 steps, with convergence on the final solution occurring within 300 steps. The first 500 steps are removed as burn-in, after which the median of the posterior distributions varies by $< 1\%$. We use linear spacing in all parameters except R_c , where we fit $\log(R_c)$. We assume uniform priors that simply restrict parameters to physically realistic values (e.g. $\delta v_{\text{turb}} > 0$, $T_{\text{atm}0} > 0$, $R_{\text{in}} > 0$).

4. RESULTS

4.1. Non-zero turbulence around DM Tau

Unlike in the disks around HD 163296 and TW Hya, we find that a non-zero turbulence provides the best fit to the disk around DM Tau, with a 99.7% confi-

Table 2. Fixed Model Parameters

Star	Stellar Mass (M_{\odot})	M_{gas} (M_{\odot})	X_{CO}	Distance (pc)	PA	Z_{q0} (au)	γ
DM Tau	0.54 (1)	0.04 (2,3)	2×10^{-5} (3)	144.5 ± 1.1 (4)	154.8°	70	1
MWC 480	1.85 (5)	0.046 (6)	10^{-4}	161.1 ± 2.0 (4)	147.8°	50	1
V4046 Sgr	1.75 (7)	0.09 (8)	3×10^{-6} (7)	72.26 ± 0.34 (4)	75.7°	35	1

References: (1) Simon, et al. (2000), (2) Andrews, et al. (2011), (3) McClure, et al. (2016), (4) Lindegren et al. (2018); Bailer-Jones et al. (2018), (5) Piétu, et al. (2007), (6) This work (7) Rosenfeld, et al. (2012), (8) Rosenfeld, et al. (2013b)

dence interval on the turbulent motion of $0.279^{+0.005}_{-0.004}c_s$ (Table 3), corresponding to velocities of 60-80 m s^{-1} . Model spectra, and residuals generated from the difference between model and data visibilities, are shown in Figure 1. Full posterior distributions, along with the progression of the walkers through the chains, are shown in appendix C. The non-zero turbulence model spectrum is well matched to the data, and outside of a persistent unresolved (diameter < 40 au) positive residual at the center, indicating that the model underestimates the data, the channel maps do not show strong residuals. As discussed below, similar central residuals are seen around MWC 480 and V4046 Sgr and may be due to deviations from our simple prescriptions for density and temperature, or a sign of changing CO abundance with radius.

The MCMC modeling indicates that a non-zero turbulence exists at a highly significant level. To verify this conclusion, we perform an additional MCMC run with the turbulence fixed at zero. This results in a model that systematically underestimates the flux of the disk (Figure 1). Comparing the median models from both trials using the Akaike Information Criterion (Akaike 1974) the difference is confirmed, with the zero turbulence model being worse than the non-zero turbulence model at a level that is much greater than 10σ . We also can confirm the non-zero turbulence by fitting to the unbinned spectra while allowing turbulence to vary. Again we find non-zero turbulence ($0.252^{+0.003}_{-0.004}c_s$) confirming our fit to the binned spectrum.

We find an uncertainty on the turbulence at the $\sim 2\%$ level, but this does not include the systematic uncertainty on the amplitude calibration, which may affect the derived temperature structure, and in turn the turbulent broadening. The 4-7% variation in amplitude measured between the short and long baseline observations of the three systems under study here is consistent with some uncertainty in the flux calibration of these data. To test the robustness of our result in the face of the amplitude calibration uncertainty, we run additional trials in which the model is systematically scaled by $\pm 20\%$, simulating

a true disk flux that is 20% fainter/brighter than is actually observed. Again we find significant turbulence, with $\delta v_{\text{turb}} = 0.300 \pm 0.005c_s$ for a faint disk and $\delta v_{\text{turb}} = 0.257^{+0.004}_{-0.005}c_s$ for a bright disk. These results differ in the gas temperature with $T_{\text{atm}0} = 21.26^{+0.09}_{-0.08}$ K for the faint disk and $T_{\text{atm}0} = 28.08^{+0.15}_{-0.12}$ K for the bright disk, which in turn affects the exact value of the sound speed. This anti-correlation between $T_{\text{atm}0}$ and δv_{turb} is also seen in the fiducial model posterior distribution (Figure 8). The range in δv_{turb} values between the systematic uncertainty models is larger than in the fiducial model since the amplitude calibration uncertainty allows for a larger range in $T_{\text{atm}0}$. The anti-correlation between δv_{turb} and $T_{\text{atm}0}$ does indicate that uncertainty in the gas temperature structure influence our turbulence constraints.

As discussed earlier, the assumed midplane temperature also influences the final turbulence result. We run an additional MCMC ensemble in which $T_{\text{mid}0}$ has been reduced to 11 K, as suggested by observations of N_2H^+ (Qi et al. 2019), and lower than employed in the chemical models of Loomis et al. (2015). Again we find non-zero turbulence, at a level of $\delta v_{\text{turb}} = 0.328 \pm 0.004c_s$. The anti-correlation between midplane temperature and turbulence arises because both influence the strength of the emission at the edges of the emitting regions within a given channel map (Flaherty, et al. 2018). These regions have low optical depth and probe the gas temperature closer to the midplane; increasing the midplane temperature will increase the intensity of the emission from these edges. At the same time, increasing turbulence will increase the amount of emission that “bleeds over” from nearby channels, leading to an increase in the optical depth and emission that arises from higher and warmer layers. As a result, a given intensity along the edges of the emission within a specific channel can be achieved with either a cold midplane and strong turbulence, or weaker turbulence and a warmer midplane. When combined with the results from the amplitude calibration trials, the low $T_{\text{mid}0}$ trial indicates that systematic uncertainties dominate over statistical uncertainties in our measurement of turbulence. Based on the sample

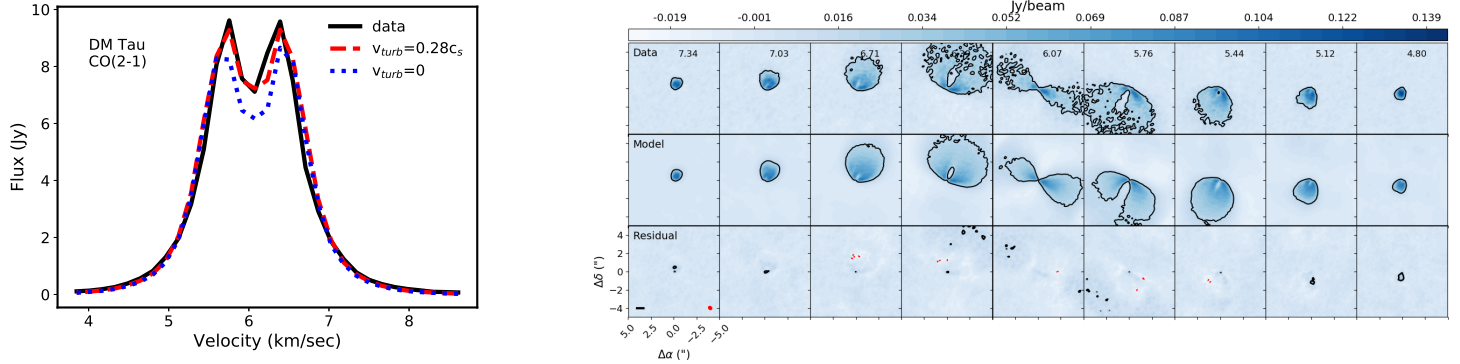


Figure 1. (Left:) Spectra of the DM Tau CO(2-1) emission (black line) and the model defined by the median of the PDFs (red-dashed line). The blue dotted line indicates a model fit in which turbulence has been fixed at zero, while the rest of the parameters are allowed to vary. The zero-turbulence fit is significantly worse than the non-zero turbulence fit. (Right:) Channel maps of the data (top row), model with non-zero turbulence (middle row), and the imaged residuals (bottom row). For the data and model frames the black contours mark the 5σ ($=22\text{mJy/beam}\sim 17\%$ of the peak flux) boundary. In the residual frames, positive (black) contours and negative (red dashed) contours are included at multiples of 5σ . The bottom left panel includes a 100 au scale bar and the synthesized beam. Here we only show the model with non-zero turbulence, which is able to reproduce nearly all of the CO emission from around DM Tau.

of trials run here, we find $\delta v_{\text{turb}} = 0.25 - 0.33c_s$, significantly larger than zero, but with a larger uncertainty than indicated by any individual trial.

Previous analysis of CS(3-2) and CS(5-4) (Guilloteau et al. 2012) found significant turbulence around DM Tau, at a level of 120 m s^{-1} , with CS being used instead of CO because of its larger molecular weight and hence smaller thermal broadening. When including the uncertainty on the turbulence velocity and the temperature structure, this translates to a 3σ range of $(0.12-0.69)c_s$, consistent with our measured range of $(0.25-0.33)c_s$ when accounting for systematic uncertainties (Figure 2). The higher signal-to-noise and higher spatial resolution ALMA data provide a tighter constraint on the turbulence around DM Tau.

Interpreting these results in the context of theoretical models requires knowledge of the emitting region of the molecular emission. Figure 2 shows the emitting region of CO derived from our models as well as that of CS from Guilloteau et al. (2012); the emission from both

4.1.1. Anisotropic vs Isotropic motion

Within our models we assume that the non-thermal non-Keplerian component of the motion is isotropic turbulence, but other forms of non-Keplerian motion may exist in protoplanetary disks. Deviations are predicted to be induced by planets (Pérez et al. 2018; Bae & Zhu 2018) and recent observational studies have found evidence for deviations from Keplerian motion due to the gravitational influence of unseen planets (Pinte et al. 2018b; Teague et al. 2018b,c; Pinte et al. 2019). Zonal flows, radial density variations associated with magnetic field concentrations, as well as the vertical shear insta-

bility (VSI), arising in part from the change in Keplerian velocity with vertical distance from the midplane, produce corrugated variations in the gas motions on velocity scales that are comparable to the non-thermal non-Keplerian motion observed around DM Tau (e.g. Simon & Armitage 2014; Flock, et al. 2017). If deviations from Keplerian motion are spread through a large region of the outer disk, and are of a sufficiently high velocity at a sufficiently small spatial scale, they may mimic the appearance of isotropic turbulence. molecules arises from between two and three pressure scale heights above the midplane. The emitting regions are at low column densities, where far ultraviolet photons are expected to ionize the disk, making it more susceptible to MRI (Perez-Becker & Chiang 2011). At $\delta v_{\text{turb}} = 0.25 - 0.33c_s$, the turbulence is at the low end for model predictions from MRI (Simon, et al. 2015; Simon et al. 2018), consistent with gravito-turbulence (Forgan et al. 2012; Shi & Chiang 2014; Shi et al. 2016), and at the high end for the vertical shear instability (Richard et al. 2016; Flock, et al. 2017). Distinguishing between these different models for the source of the turbulence may require a measure of the vertical structure of the turbulence (Simon, et al. 2015), more detailed knowledge of the physical conditions within the outer disk (Lyra & Umurhan 2019; Simon et al. 2018), or complementary observations of other disk properties that are influenced by the turbulence (e.g. dust settling Flock, et al. 2017)

bility (VSI), arising in part from the change in Keplerian velocity with vertical distance from the midplane, produce corrugated variations in the gas motions on velocity scales that are comparable to the non-thermal non-Keplerian motion observed around DM Tau (e.g. Simon & Armitage 2014; Flock, et al. 2017). If deviations from Keplerian motion are spread through a large region of the outer disk, and are of a sufficiently high velocity at a sufficiently small spatial scale, they may mimic the appearance of isotropic turbulence.

To test the sensitivity of our data to structured motion, we employ a toy model in which we add a velocity

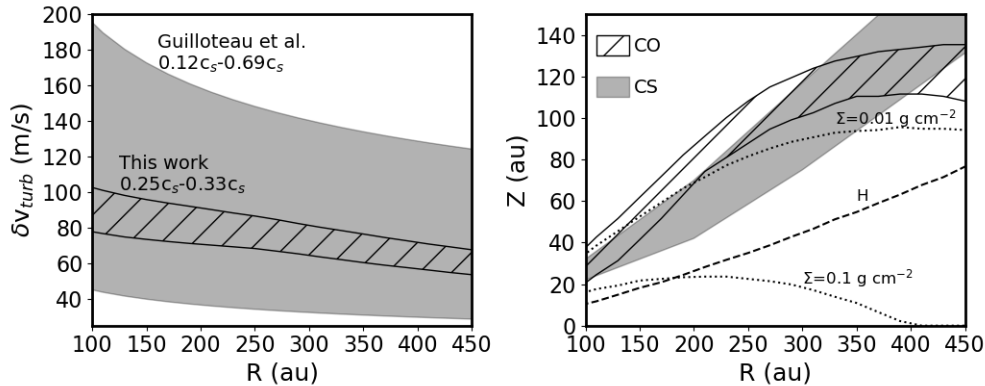


Figure 2. (Left) Turbulence levels as a function of radius in the disk around DM Tau, as derived from CS (Guilloteau et al. (2012), wide grey band) and CO (this work, narrow hatched band). For the Guilloteau et al. (2012) results we show the 3σ range, including the uncertainty on both the derived turbulence and the gas temperature (when deriving turbulence as a function of the sound speed), while in the results from this work we include systematic uncertainties. Our results are consistent with the previous measurements, albeit with smaller uncertainties. (Right) Molecular emitting regions for CO (this work) and CS (Guilloteau et al. 2012). Both molecules are probing similar regions, at one to three pressure scale heights (H) above the midplane.

component in the orbital direction that varies as a function of radius:

$$dv_\phi = dv \sin\left(\frac{2\pi R}{dR}\right) \quad (7)$$

Here dv represents the maximum deviation from Keplerian motion, while dR is the spatial scale of the perturbation. This perturbation is added to a model with parameters ($T_{\text{atm}0}$, R_c , etc.) based on the DM Tau fiducial model. Visibilities are generated from the model images, and are used to create a cleaned image, using the same procedure as for the data.

In Figure 3 we show the central velocity channel of three models: (1) large spatial scale and high velocity ($dR=150$ au, $dv=1.5$ km s^{-1}), (2) small spatial scale and high velocity ($dR=70$ au, $dv=1.5$ km s^{-1}), and (3) large spatial scale and small velocity ($dR=150$ au, $dv=0.3$ km $s^{-1} \sim c_s$). Anisotropic motion is easily distinguishable from isotropic turbulence in the large size scale and large velocity model due to the corrugated emission structure but becomes more difficult to detect as the size and velocity scales become smaller. When the distance between the minimum and maximum velocity deviation ($dR/2$) becomes smaller than the beam size (~ 40 au for DM Tau) the features are no longer spatially resolved, and blend together into a general broadening of the emission. For small velocity scales the azimuthal perturbations to the image are small enough that they are not resolvable as distinct features. Leveraging the full three-dimensional data cube, rather than a single channel as shown in Fig 3, provides greater sensitivity to smaller fluctuations (Teague et al. 2018b,c), although is still limited by the spatial resolution of the data.

Theoretical models of structured non-Keplerian motion suggest that the radial and velocity scales of typical features are small enough to make them difficult to distinguish from purely isotropic motion in our data. The size scale of these features generally scale with the pressure scale height (H) and for DM Tau our model fits indicate a pressure scale height that reaches 70 au at 500 au from the central star. With a beam size of ~ 40 au, features as large as (5-10)H would be easily resolved. Global non-ideal MHD simulations find that when the net poloidal field is relatively strong (thus driving high accretion rates), the disk tends to form zonal flows of scales¹ of $\sim 2H$ (Béthune et al. 2017; Suriano et al. 2018), while in shearing box simulations, zonal flows are found at a broader range of disk magnetizations, on scales of 4H or beyond and is dependent on the box size (Bai & Stone 2014; Simon & Armitage 2014) and the magnetization of the disk (Riols, & Lesur 2019). Vertical shear instabilities produce corrugated variations in the gas motion with velocities of 10-20% of the local sound speed and size scales of $\sim 2H$ (Flock, et al. 2017). At these scales, zonal flows and VSI are difficult to distinguish from isotropic motion in our data, although other factors, such as the efficient lifting of dust grains by VSI (Flock, et al. 2017) may break this degeneracy. Planet

¹ The cited papers typically discuss the size scale of individual features, e.g. the radial size of a region with higher than Keplerian motion, which corresponds to $dR/2$ in the context of our toy model. In comparing with our sensitivity tests, we quote size scales that are consistent with our definition of dR , and hence are typically twice as large as the values mentioned in the cited papers.

Table 3. CO(2-1) Model results

Model	q	$\log(R_c(\text{au}))$	$\delta v_{\text{turb}} (c_s)$	$T_{\text{atm0}} (K)$	$T_{\text{mid0}} (K)$	inclination ($^\circ$)	$R_{\text{in}} (\text{au})$	$v_{\text{sys}} (\text{km s}^{-1})$
DM Tau								
Fiducial	$-0.371^{+0.003}_{-0.002}$	$2.444^{+0.004}_{-0.003}$	$0.279^{+0.005}_{-0.004}$	$24.68^{+0.11}_{-0.09}$	14.3 ^a	$36.0^{+0.12}_{-0.09}$	<9	6.017 ± 0.001
sys=1.2	-0.344 ± 0.003	$2.452^{+0.003}_{-0.004}$	$0.257^{+0.004}_{-0.005}$	$28.08^{+0.15}_{-0.12}$	14.6 ^a	$36.21^{+0.12}_{-0.13}$	<9	$6.018^{+0.001}_{-0.002}$
sys=0.8	$-0.403^{+0.003}_{-0.002}$	2.44 ± 0.01	0.300 ± 0.005	$21.26^{+0.09}_{-0.08}$	14.0 ^a	$35.81^{+0.12}_{-0.13}$	<9	6.016 ± 0.001
highres	$-0.352^{+0.001}_{-0.002}$	2.440 ± 0.002	$0.252^{+0.003}_{-0.004}$	$24.92^{+0.08}_{-0.07}$	14.5 ^a	$35.99^{+0.09}_{-0.08}$	<9	6.045 ± 0.001
$\delta v_{\text{turb}}=0$	$-0.352^{+0.004}_{-0.002}$	$2.456^{+0.004}_{-0.003}$	0 ^b	27.54 ± 0.09	14.5 ^a	$37.73^{+0.16}_{-0.11}$	<9	$6.013^{+0.002}_{-0.001}$
low T_{mid0}	$-0.310^{+0.002}_{-0.003}$	$2.469^{+0.004}_{-0.005}$	0.328 ± 0.004	$25.57^{+0.09}_{-0.07}$	11.0 ^c	35.86 ± 0.11	<9	6.019 ± 0.001
MWC 480								
Fiducial	-0.467 ± 0.002	$2.161^{+0.004}_{-0.001}$	<0.12	$60.3^{+0.3}_{-0.2}$	18.8 ^b	$-40.34^{+0.05}_{-0.06}$	<9	5.102 ± 0.001
highres	-0.457 ± 0.002	$2.172^{+0.002}_{-0.001}$	<0.08	62.1 ± 0.2	18.8 ^b	$-40.37^{+0.05}_{-0.04}$	<9	5.137 ± 0.001
$\delta v_{\text{turb}}=0$	-0.463 ± 0.002	$2.168^{+0.002}_{-0.003}$	0 ^b	62.3 ± 0.1	18.8 ^b	$-40.49^{+0.06}_{-0.05}$	<9	5.102 ± 0.001
low T_{mid0}	$-0.413^{+0.001}_{-0.003}$	$2.208^{+0.004}_{-0.003}$	<0.18	$70.02^{+0.36}_{-0.05}$	14 ^b	-40.06 ± 0.05	<9	5.141 ± 0.001
V4046 Sgr								
Fiducial	-0.565 ± 0.003	$1.939^{+0.004}_{-0.003}$	<0.15	$27.84^{+0.13}_{-0.09}$	12 ^b	$34.69^{+0.03}_{-0.04}$	<7	2.857 ± 0.001
highres	$-0.564^{+0.003}_{-0.001}$	$1.939^{+0.001}_{-0.003}$	<0.12	$28.26^{+0.10}_{-0.05}$	12 ^b	$34.68^{+0.02}_{-0.03}$	<7	$2.8957^{+0.0005}_{-0.0006}$
$\delta v_{\text{turb}}=0$	-0.579 ± 0.002	$1.956^{+0.004}_{-0.003}$	0 ^b	$28.80^{+0.04}_{-0.07}$	12 ^b	$34.76^{+0.04}_{-0.03}$	<7	$2.857^{+0.001}_{-0.001}$
low T_{mid0}	$-0.565^{+0.002}_{-0.004}$	$2.078^{+0.012}_{-0.002}$	<0.18	$29.27^{+0.17}_{-0.06}$	8 ^b	$34.59^{+0.05}_{-0.03}$	<6.5	2.857 ± 0.001

sys=1.2: A trial simulating if the data were systematically 20% brighter than measured, *sys=0.8*: A trial simulating if the data were systematically 20% fainter than measured, *highres*: A trial fitting to the data at full spectral resolution, rather than the binned spectra used in the fiducial model, $v_{\text{turb}}=0$: A trial in which turbulence is fixed at zero, *low T_{mid0}* : A trial in which the midplane gas temperature is lower than the fiducial model.

^a $T_{\text{mid0}} = 19(70/150)^{-q}$. This forces the midplane temperature to 19 K at 70 au, matching the location of the CO condensation front in the chemical modeling of Loomis et al. (2015)

^b Held fixed during the fitting process.

^c $T_{\text{mid0}} = 14(70/150)^{-q}$.

induced motions are unlikely to be mis-interpreted as turbulence because of the highly localized nature of the perturbation (Pérez et al. 2018). In modeling the CO emission from around DM Tau we assume that a single turbulence value, relative to the local sound speed, applies uniformly throughout the disk. The residuals do not show a strong deviation from this assumption, outside of the unresolved emission at the center of the disk. This suggests that instabilities that generate features over a wide radial range within the disk, such as is possible under certain physical conditions with zonal flows and vertical shear instabilities, as well as MRI assuming the surface layers are sufficiently ionized, are consistent with our results around DM Tau.

4.2. Weak Turbulence around MWC 480 and V4046 Sgr

For both the disk around MWC 480 and the disk around V4046 Sgr we do not detect significant nonthermal motion of the gas. Figures 4 and 5 show the data as

compared to the model defined by the median of the posterior distributions (posterior distributions are shown in Appendix C). For both MWC 480 and V4046 Sgr, the MCMC routine returns a posterior that nominally indicates a detection of turbulence. We run additional trials with turbulence fixed at zero and find that the zero turbulence fit is nearly indistinguishable, in both the spectra and the channel maps, from the non-zero turbulence result, although as discussed below there are still residuals between the best fit models and the data. For this reason we conservatively interpret the results for MWC 480 and V4046 Sgr as upper limits rather than detections.

For MWC 480, we are able to constrain turbulence to $<0.12c_s$. Fitting to the un-binned data pushes the limit down to $<0.08c_s$, corresponding to velocities below 20-40 m s^{-1} beyond 100 au. For V4046 Sgr a fit to the binned spectrum constrains turbulence to $<0.15c_s$, while a fit to the un-binned spectrum pushes the upper limit down to $<0.12c_s$, corresponding to velocities

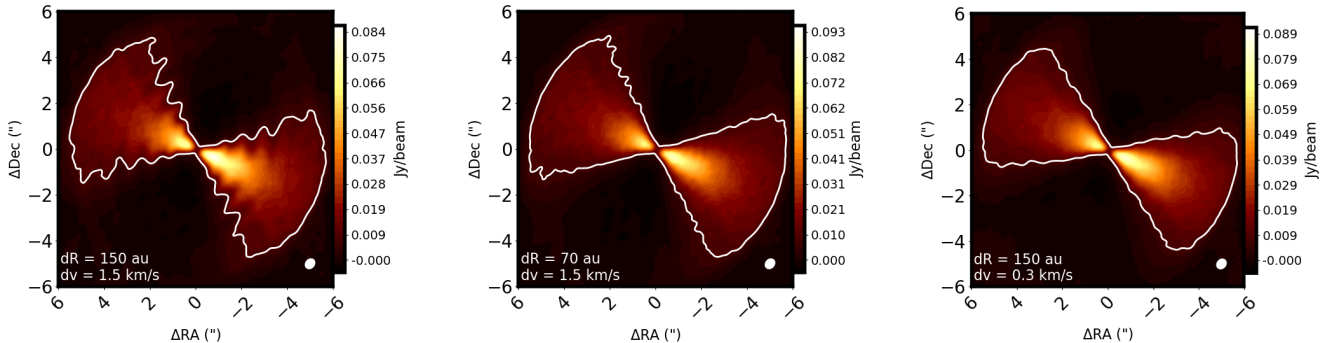


Figure 3. Simulated images of the central velocity channel for a radial variation in azimuthal velocity. For features with large velocities and large size scales ($dR=150$ au, $dv = 1.5$ km s $^{-1}$, left panel), the anisotropic motion displays a corrugated pattern in the images. When the size scale of the features is small ($dR = 70$ au, center panel) the features are unresolved and appear as a general broadening of the image. When the velocity scale of the features is small ($dv=0.3$ km s $^{-1} \sim c_s$, right panel) corrugated features can be difficult to detect even though they are spatially resolved. This indicates that it is difficult for us to distinguish isotropic turbulence from anisotropic motion below the sound speed and at size scales below the resolution of the observations.

below 30-55 m s $^{-1}$ beyond 100 au. As with DM Tau, we consider models with colder midplane temperatures ($T_{\text{mid}0} = 14$ K for MWC 480, and 8 K for V4046 Sgr) and in both cases the upper limits rise to $<0.18 c_s$, but are still consistent with a non-detection of turbulence. This suggests that systematic effects (e.g., the assumed midplane temperature) are significant compared to statistical uncertainties when constraining the turbulence level in these systems.

In the case of both MWC 480 and V4046 Sgr, the imaged residuals show structure (Figure 4, 5), although at a level that is less than 10% of the peak flux. Both systems show an unresolved positive residual at the center of the disk, with a diameter <50 au and <20 au for MWC 480 and V4046 Sgr respectively, which may be a result of a deviation from simple prescriptions for the temperature and surface density radial profiles, a change in CO abundance with radius (e.g. Schwarz et al. 2018), or a change in the velocity profile due to a warp (e.g. Walsh et al. 2017) or rapid inward radial flow (e.g. Rosenfeld et al. 2014). Around V4046 Sgr negative residuals extend out to ~ 200 au, corresponding to the radius beyond which our simple photo-desorption treatment sets the CO abundance. This suggests that a more detailed treatment of photodesorption would bring the model in closer agreement with the data. None of these residuals are indicative of an underestimate of the turbulence level. In the channel maps turbulence acts to broaden emission rather than to change the radial profile (Simon, et al. 2015). Also, the similarity between the model derived when turbulence was fixed at zero versus the model derived when turbulence was allowed to vary supports our interpretation of the model results as an upper limit. We can rule out turbulence levels comparable to that around DM Tau, but cannot com-

pletely rule out modest turbulent motions within these systems.

5. DISCUSSION

5.1. Is weak turbulence common among planet-forming disks?

Based on an analysis of CO(2-1) ALMA observations of the disks around DM Tau, MWC 480, and V4046 Sgr we find significant non-zero turbulence around DM Tau, but only upper limits for the disks around MWC 480 and V4046 Sgr, similar to what has been found in the disks around HD 163296 (Flaherty et al. 2015, 2017) and TW Hya (Flaherty, et al. 2018; Teague et al. 2018a).

Molecular line emission provides a direct measure of gas motions, but it is not the only tracer of turbulence in the outer disk. Strong turbulence will loft dust grains away from the disk midplane (Youdin & Lithwick 2007; Turner et al. 2010), making dust settling an indirect tracer of turbulence, in particular the turbulence at the midplane of the disk. Using the influence of dust settling on the SED, Boneberg, et al. (2016) find $\alpha \sim (0.1 - 6.3) \times 10^{-3}$ around HD 163296, while Mulders & Dominik (2012) use the average SEDs of T Tauri stars, Herbig stars, and brown dwarfs and find $\alpha=10^{-4}$ is a better fit to the data than $\alpha=10^{-2}$, for regions of the disk within ~ 100 au of the central star. In combining scattered light observations and the SED, van Boekel, et al. (2017) find $\alpha \sim 2 \times 10^{-4}$ around TW Hya. Qi et al. (2019) find that, in SED fitting and comparison with the N $_2$ H $^+$ emission morphology, the disk around V4046 Sgr exhibits more dust settling, and hence has weaker turbulence, than the disk around DM Tau, consistent with our results.

High resolution images of gaps in planet-forming disks have opened up additional probes of turbulence through

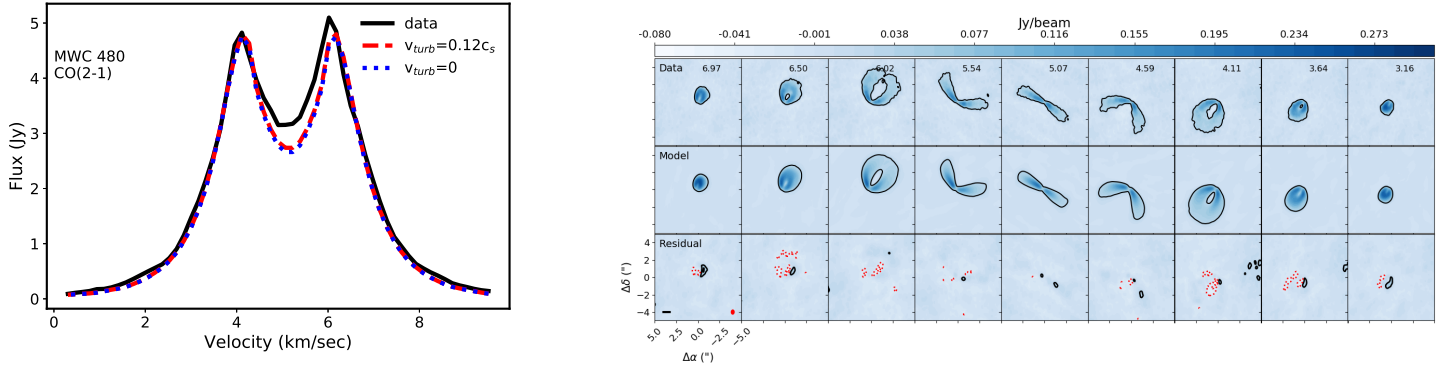


Figure 4. (Left:) Spectra of the MWC480 CO(2-1) emission (black line) and the model defined by the median of the PDFs when turbulence is allowed to vary (red dashed line) as well as when turbulence is fixed at zero (blue dotted line). (Right:) Channel maps of the data (top row), model (middle row), and residuals (bottom row). The contour in the data and model frames is at 5σ ($=29\text{mJy/beam}\sim 10\%$ of the peak flux), while the contours in the residual frame are at multiples of 5σ .

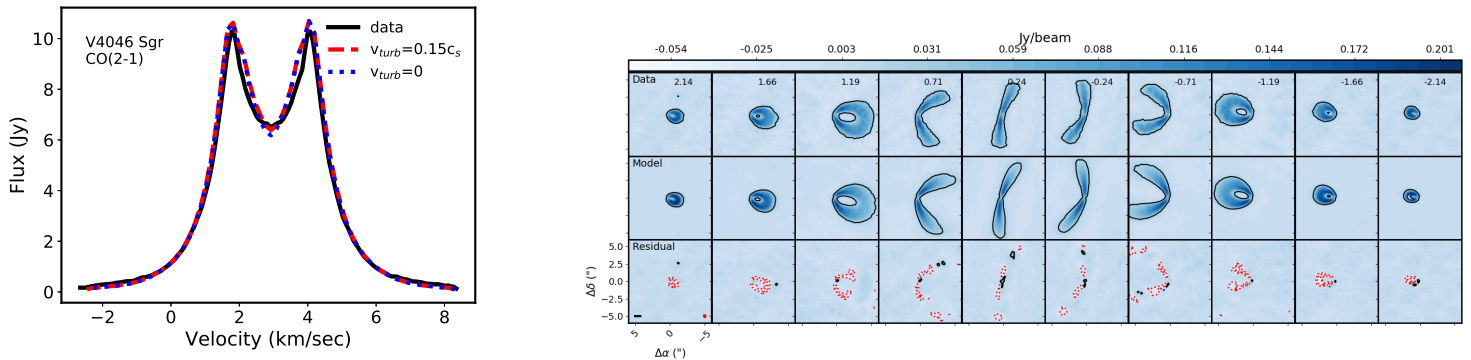


Figure 5. (Left:) Spectra of the V4046 CO(2-1) emission (black line) and the model defined by the median of the PDFs when turbulence is allowed to vary (red dashed line) as well as when turbulence is fixed at zero (blue dotted line). (Right:) Channel maps of the data (top row), model (middle row), and residuals (bottom row). The contour in the data and model frames is at 5σ ($=24\text{mJy/beam}\sim 7\%$ of the peak flux), while the contours in the residual frame are at multiples of 5σ .

the effect of turbulence on the appearance of dust and gas gaps. The well defined dust gaps around HL Tau are a sign of substantial dust settling, as expected for $\alpha \sim 10^{-4}$ (Pinte, et al. 2016). Using hydrodynamic simulations of gas and dust gap formation via gravitational interactions with massive planets, Liu et al. (2018) find that α increases with radius from $<10^{-4}$ to 8×10^{-3} in the disk around HD 163296, while Ohashi & Kataoka (2019) find that the polarization pattern is also consistent with a rise in α , although at a factor of ten higher level ($\alpha \lesssim 1.5 \times 10^{-3}$ at 50 au rising to 0.015-0.3 at 90 au). In high resolution ALMA images the disks around AS 209, DoAr 25, Elias 20, and RU Lup (Huang et al. 2018) and HD 169142 (Pérez et al. 2019) exhibit ‘double gap’ features consistent with clearing by a single planet in a low viscosity disk ($\alpha < 10^{-4}$ Dong et al. 2017). Overall, while observations are limited to the brightest systems, they suggest that large turbulence is not a frequent occurrence around protoplanetary disks at least in the mid-plane.

In the context of the α -disk model, turbulent velocities from molecular line observations can be converted to α via $\alpha \sim (\delta v_{\text{turb}}/c_s)^2$, but caution is needed when comparing to α values derived in different observational studies, as well as α values from numerical simulations. Direct conversion from turbulent velocities to α values results in $\alpha = 0.078 \pm 0.002$ for the disk around DM Tau, $\alpha < 0.006$ for disk around MWC 480 and $\alpha < 0.01$ for the disk around V4046 Sgr. These α values only apply to the localized region where the CO emission arises, which is well above the midplane (e.g. Figure 2). Observations of millimeter dust continuum emission will be more sensitive to the turbulence at smaller radii than the gas, since dust emission is often more compact than gas emission (e.g. Kastner et al. 2018), and at the midplane, in part because large grains quickly settle to the midplane and because the scale height of the dust is most sensitive to the turbulence near the midplane (Ciesla 2007). If the turbulence varies with vertical height, as is expected for MRI driven turbulence, the local α value will change

with height as well. For example, in an MRI simulation at 100 au from [Simon, et al. \(2015\)](#) with an initial gas to magnetic pressure ratio at the midplane of $\beta_0=10^5$ and an FUV penetration depth of $\Sigma_{\text{FUV}}=0.01 \text{ g cm}^{-2}$ the turbulent velocity varies with height by a factor of ~ 10 ($0.7c_s$ at 3 pressure scale heights vs. $0.04c_s$ at the midplane), resulting in a factor of ~ 100 difference between the local α values ($\alpha=0.49$ at 3 pressure scale heights vs. 0.002 at the midplane). These local α values are distinct still from the density-weighted average of the stress tensor ($\alpha=0.0026$), which is related to the accretion flow through the disk and is weighted more strongly toward the high density midplane. Measurements of the turbulence near the midplane through optically thin molecular line tracers or dust observations, in addition to confirmation that the measured non-thermal motion around DM Tau is due to turbulence and not unresolved structured motion, are needed to fully characterize the α -viscosity in these systems.

5.2. Physical conditions for turbulence

Physical conditions within the disk can set the turbulence level and may explain the lack of turbulence among many of the studied sources. In the context of MRI, [Simon et al. \(2018\)](#) explore the turbulence levels among models with different ionization conditions and magnetic field strengths. They find that the presence of FUV emission drives strong turbulence ($0.2c_s$ - $0.7c_s$), while the removal of this ionization component, especially when combined with weak magnetic fields, can lead to weak turbulence ($0.02c_s$ - $0.09c_s$). Among the sources with constraints on turbulence from molecular line emission, DM Tau exhibits the weakest FUV flux (Table 4) despite having the only turbulent disk. X-ray emission can also ionize gas, but again DM Tau does not possess the strongest X-ray emission among our sample. This suggests that FUV and X-ray emission strength alone does not set the turbulence level.

Observations constrain the FUV and X-ray emission near the stellar surface, while the relevant parameter for MRI models is the FUV and X-ray field as seen by material in the outer disk. High energy radiation can be severely attenuated before reaching the outer disk if intervening material, such as a wind launched by the inner disk, acts as an obscuring screen. TW Hya ([Pascucci et al. 2011](#)), MWC 480 ([Fernandes et al. 2018](#)), V4046 Sgr ([Sacco, et al. 2012](#)), and HD 163296 ([Klaassen et al. 2013](#)) show evidence of a disk wind based on optical/infrared forbidden lines (TW Hya, V4046 Sgr), infrared emission (MWC 480), and extended CO emission (HD 163296). In contrast, the optical forbidden line emission from DM Tau can be explained entirely

with a gas disk in Keplerian motion ([Simon et al. 2016](#)). Whether or not a wind is the defining factor between a turbulent and non-turbulent disk depends on the density of the wind, with vertical column densities of 0.01 g cm^{-2} sufficient to absorb a majority of the FUV radiation ([Perez-Becker & Chiang 2011](#)).

Regardless of the ionizing source, the ionization level of the outer disk can be constrained based on observations of ionized molecular species. The presence of e.g. DCO^+ , HCO^+ , N_2H^+ in the outer disk of HD 163296 ([Flaherty et al. 2017](#)), TW Hya ([Qi et al. 2013](#)), DM Tau ([Dutrey et al. 1997](#); [Öberg et al. 2011](#); [Teague et al. 2015](#)), MWC 480 ([Öberg et al. 2010](#); [Huang et al. 2017](#)) and V4046 Sgr ([Öberg et al. 2011](#); [Huang et al. 2017](#)) suggests that some ionizing radiation reaches the outer disk. [Öberg et al. \(2011\)](#) measure an ionization fraction of $\sim 4 \times 10^{-10}$ in the CO layer around DM Tau, comparable to the ionization fraction in the models from [Simon et al. \(2018\)](#) that assumed no FUV photons but still included X-rays and cosmic-rays. A subset of these models displayed vigorous turbulence in the upper disk layers.

[Cleeves et al. \(2017\)](#) found that the H^{13}CO^+ abundance around IM Lup varied in response to an X-ray flare, indicating that the ionization level may change on short timescales. In the presence of variable ionization, MRI will respond with varying turbulence levels on its growth/decay timescale. Since the MRI relies on the differential rotation of gas, its growth/decay timescale is, at its fastest, the dynamical timescale of the gas. Molecular line observations with ALMA probe regions of the disk beyond ~ 30 au, corresponding to dynamical timescales of hundreds to thousands of year. In their chemical modeling, [Cleeves et al. \(2017\)](#) find that the HCO^+ abundance would be enhanced for 10-20 days at 100 au following an X-ray flare, much shorter than the time needed for MRI to respond to changes in the ionization, resulting in little variation in turbulence with time. Longer timescale fluctuations in e.g. the wind mass loss rate may still lead to oscillations in the turbulence level over the course of the disk lifetime.

For reasonable values of the magnetic field strength, as informed by theoretical models (e.g. [Bai & Stone 2011](#); [Bai 2016](#); [Simon et al. 2018](#)), stronger fields generally result in stronger turbulence, and possibly higher accretion rates. The predicted correlation between turbulence and accretion rate seems to be contradicted in our sample, with DM Tau showing the strongest turbulence at yet the weakest accretion rate. This may be due to the fact that the measured accretion rate is the instantaneous accretion rate onto the star, and does not reflect the accretion rate in the outer disk where the

Table 4. System properties

Star	δv_{turb}	M_*	M_{disk}	Age	\dot{M}_{acc}	$L_{\text{X-ray}}$	L_{FUV}
		M_{\odot}	M_{\odot}	Myr	$M_{\odot} \text{ yr}^{-1}$	L_{\odot}	L_{\odot}
HD 163296	$<0.05c_s$ (1)	2.3	0.09 (2)	5	5×10^{-7} (3)	10^{-4} (4, 5)	3.21-5.58 (6)
TW Hya	$<0.08c_s$ (7)	0.6	0.05 (8)	10-12	2×10^{-9} (9, 10, 11)	6.8×10^{-4} (12, 13, 14, 15)	7×10^{-3} (16)
MWC 480	$<0.08c_s$ (17)	1.85 (18)	0.046 (17)	7-8	5.3×10^{-7} (19, 3, 20)	2.6×10^{-6} (21)	...
V4046 Sgr	$<0.12c_s$ (17)	0.9, 0.9	0.09 (22)	12-23 (23, 24, 25)	1.3×10^{-8} (26)	3.1×10^{-4} (27, 28)	10^{-2} (16)
DM Tau	$0.25\text{-}0.33c_s$ (17)	0.54 (29)	0.04 (30,31)	1-5	2.9×10^{-9} (16, 32)	7.8×10^{-5} (33)	3×10^{-3} (34, 16)
Typical Disk Ranges	3×10^{-4} - 0.03 (35)	1-10	5×10^{-11} - 10^{-7} (36)	2×10^{-6} - 0.02 (37)	2×10^{-3} - 0.2 (16)

References: (1) Flaherty et al. (2017) (2) Isella, et al. (2007), (3) Mendigutía, et al. (2013), (4) Günther & Schmitt (2009), (5) Swartz, et al. (2005), (6) Meeus, et al. (2012), (7) Flaherty, et al. (2018), (8) Bergin, et al. (2013), (9) Alencar & Batalha (2002), (10) Herczeg, et al. (2004), (11) Ingleby, et al. (2013), (12) Brickhouse, et al. (2010), (13) Dupree, et al. (2012), (14) Kastner, et al. (1999), (15) Kastner, et al. (2002), (16) France, et al. (2014), (17) This work, (18) Piétu, et al. (2007) (19) Costigan, et al. (2014), (20) Donehew & Brittain (2011), (21) Henning, et al. (2010), (22) Rosenfeld, et al. (2013b), (23) Mamajek & Bell (2014) (24) Torres, et al. (2006), (25) Binks & Jeffries (2014), (26) Curran, et al. (2011), (27) Espaillat, et al. (2013), (28) Sacco, et al. (2012), (29) Simon, et al. (2000), (30) Andrews, et al. (2011), (31) McClure, et al. (2016), (32) Ingleby, et al. (2011), (33) Cleeves, private communication, (34) Yang, et al. (2012), (35) Andrews, et al. (2013), (36) Manara, et al. (2016), (37) Feigelson, et al. (2005)

turbulence is measured, or that the turbulence signature does not reflect MRI-generated turbulence but instead reflects other sources of non-thermal motion (e.g., unresolved spatial variations in azimuthal velocity).

Age may also play a factor in the strength of the turbulence by driving the evolution of the physical conditions that set the turbulence level. DM Tau is one of the youngest targets within our sample; as a member of the Taurus star forming region its age likely lies between 1 Myr (Luhman et al. 2010) and 5 Myr (Simon, et al. 2000; Guilloteau et al. 2014). Larger turbulence at younger ages is consistent with the findings of Najita & Bergin (2018) of large α values among class I objects. But ages of individual objects are difficult to constrain; DM Tau and MWC 480 are both part of the Taurus region, and would be expected to have similar ages, yet MWC 480 is typically assumed to be older than DM Tau (Simon, et al. 2000). Accounting for internal magnetic fields can push stellar ages to systematically higher values (Simon et al. 2019). Similarly, the lack of turbulence around the class I object HL Tau (Pinte, et al. 2016) suggests that not all objects of the same age have the same turbulence properties.

In the absence of MRI, other processes may drive turbulence under the right conditions. Forgan et al. (2012) find that gravitational instabilities can drive large scale accretion, with the driving source transitioning from large scale spiral arms to gravito-turbulence as the disk mass decreases. The measured disk masses (Table 4) are 4-8% of the stellar mass, resulting in minimum Toomre Q values of 5-15, inconsistent with the presence of gravito-turbulence. Powell et al. (2019) derive larger disk masses for HD 163296 and TW Hya based on the structure of the dust emission, but they find that even these large masses do not push these disks into the grav-

itationally unstable regime. The weak levels of turbulence may also open up the possibility of hydrodynamic instabilities, which can produce $\alpha \sim 10^{-4} - 10^{-3}$, playing a larger role (e.g. Vertical Shear Instability, Convective Overstability, and Zombie Vortex Instability as reviewed by Lyra & Umurhan 2019). The Vertical Shear Instability (VSI) develops due to the change in orbital velocity with vertical height within a disk that has sufficiently rapid cooling (Simon & Armitage 2014; Flock, et al. 2017), conditions that are likely in the outer disk (Lin & Youdin 2015). VSI can operate in a magnetized disk (Cui & Bai 2019), and produces highly anisotropic motion, dominated by vertical motion reaching 10-20% of the local sound speed (Flock, et al. 2017). Such motions can be ruled out for some of the sample HD 163296, TW Hya, MWC 480). Relying on the ability of turbulence to spread dust in the radial direction, Dullemond et al. (2018) use the resolved widths of narrow dust rings around AS 209, Elias 24, HD 163296, GW Lup, and HD 143006 to rule out $\alpha \ll 5 \times 10^{-4}$ for grain sizes $\gg 0.1$ cm, suggesting that some modest level of turbulence may exist in these systems.

6. CONCLUSION

Using new ALMA observations of CO(2-1) emission, we detect turbulence around DM Tau at a level of $\delta v_{\text{turb}} = 0.279^{+0.005}_{-0.004} c_s$, although this range extends from $0.25c_s$ to $0.33c_s$ when accounting for systematic effects (e.g., assumptions about the midplane temperature). Around MWC 480 and V4046 Sgr we find no strong evidence for non-zero turbulence, restricting the turbulence levels to $<0.08c_s$ and $<0.12c_s$ respectively. The finding of larger turbulence around DM Tau than around V4046 Sgr is consistent with the enhanced dust settling in the

disk around V4046 Sgr relative to the disk around DM Tau (Qi et al. 2019).

The upper limits on turbulence in the disks around MWC 480 and V4046 Sgr put them at a turbulence level similar to that around HD 163296 (Boneberg, et al. 2016; Flaherty et al. 2017; Liu et al. 2018; Dullemond et al. 2018) and TW Hya (van Boekel, et al. 2017; Flaherty, et al. 2018; Teague et al. 2018a). While this is still a modest sample, the results are consistent with studies of high resolution images of continuum emission, sensitive to disk properties closer to the midplane and smaller radii than the CO emission, which found modest turbulence among additional planet-forming systems ($\alpha \sim 10^{-4}$, Pinte, et al. 2016; Huang et al. 2018; Pérez et al. 2019), suggesting that weak turbulence may be a common feature among planet-forming disks. At the same time the robust detection of turbulence around DM Tau provides an important anchor point in comparison with models of instabilities within planet-forming disks.

Amongst this small sample we can begin to look for clues as to the explanation for these results. In the context of MRI, the strength of the ionizing radiation reaching the outer disk and the magnetic field are two defining factors (e.g. Simon et al. 2018). While the FUV and X-ray flux emitted by DM Tau is not large relative to MWC 480, V4046 Sgr, HD 163296, or TW Hya, DM Tau is the only source among this sample that does not show evidence for an inner disk wind that could potentially block the ionizing radiation from reaching the outer disk. The presence of ionized molecular species in all of these systems indicate that some modest level of ionization exists in the outer disk, although the exact ionization level has only been quantified in the case of the disk around DM Tau. Instead the magnetic field strength may be the

defining factor in setting the strength of the turbulence. Magnetic field strengths remain largely unconstrained, with observational upper limits (e.g. Vlemmings et al. 2019) still lying above the levels examined by theoretical models. Age also may play a role, given that DM Tau is the youngest source among our sample, although further measurements are needed to determine if this trend holds up.

The work of KMF was performed in part at the Aspen Center for Physics, which is supported by the National Science Foundation grant PHY-1607611. A.M.H. is supported by a Cottrell Scholar Award from the Research Corporation for Science Advancement. This paper makes use of the following ALMA data: ADS/JAO.ALMA#2016.1.00724.S. ALMA is a partnership of ESO (representing its member states), NSF (USA) and NINS (Japan), together with NRC (Canada), MOST and ASIAA (Taiwan), and KASI (Republic of Korea), in cooperation with the Republic of Chile. The Joint ALMA Observatory is operated by ESO, AUI/NRAO and NAOJ. The National Radio Astronomy Observatory is a facility of the National Science Foundation operated under cooperative agreement by Associated Universities, Inc. This project has received funding from the European Research Council (ERC) under the European Union’s Horizon 2020 research and innovation programme under grant agreement No 716155 (SACCRED).

Facilities: ALMA

Software: astropy (Astropy Collaboration et al. 2013), EMCEE (Foreman-Mackey et al. 2013), MIRIAD

APPENDIX

A. CO PHOTO-DESORPTION

To incorporate CO in regions with photo-desorption into our parametric structure, without resorting to detailed chemical models, we compare the timescales for freeze-out, photo-desorption and photodissociation. Regions in which photo-desorption operates more quickly than freeze-out and photo-dissociation will provide additional CO emission in the outer disk. Regions in which freeze-out or photo-dissociation dominate will be heavily depleted in CO, and will not contribute CO emission.

The freeze-out timescale is set by the frequency at which CO molecules collide with dust particles (Flower et al. 2005).

$$\tau_{fre} = (n_g \pi a_g v_{th} S)^{-1}, \quad (A1)$$

where n_g is the number density of grains, a_g is the radius of a grain particle, v_{th} is the thermal velocity of the gas, and S is the sticking efficiency, assumed to be 1.

CO photo-desorption is influenced by the UV radiation field, its ability to penetrate the disk, and the intrinsic efficiency with which CO desorbs from a dust grain in response to an incoming photon:

$$R = I_{ISRF} \exp(-\gamma A_V) Y_{pd} a_g \quad (A2)$$

where R is the number of CO molecules that are photo-desorbed per second per dust grain, I_{ISRF} is the interstellar radiation field ($=1 \text{ Habing} = 10^8 \text{ photons s}^{-1} \text{ cm}^{-2}$ Habing 1968), γ is a measure of the UV extinction relative to the visual extinction (~ 2 for small dust grains), A_V is the visual extinction, and Y_{pd} is the experimentally measured number of photo-desorptions per UV photon. A detailed calculation of the interstellar radiation field would involve accounting for the nearby stellar population (e.g. Cleeves et al. 2016), while here we assume a radiation field of 1 Habing for simplicity. The factor Y_{pd} can vary by ~ 3 -4 depending on the exact shape of the incident spectrum (Fayolle et al. 2011; Chen et al. 2014) and the temperature at which the ice is deposited on the dust grains (Öberg et al. 2009), although we ignore these effects in our calculation, and assume $Y_{\text{pd}} = 2.7 \times 10^{-3}$. Given the photo-desorption rate (R), the timescale to double the CO density is:

$$\tau_{pde} = \frac{n_{\text{CO}}}{R n_g} \quad (\text{A3})$$

where n_{CO} is the number density of CO molecules.

Once CO is released from the grains it must survive as a molecule, without being dissociated by the same UV radiation field that released it from the dust grain in the first place. The rate at which CO is photo-dissociated is (Visser et al. 2009):

$$k = \chi k_0 \Theta \exp(-\gamma A_V) \quad (\text{A4})$$

where χ is the radiation field in units of the Draine (1978) field (which corresponds to roughly 1.7 Habings), k_0 is the unattenuated photo-dissociation rate ($= 2.592 \times 10^{-10}$, in units of photo-dissociations per second per CO molecule), and Θ is the attenuation factor accounting for shielding of the radiation field by H_2 as well as self-shielding by CO. The photo-dissociation timescale is simply $\tau_{pdi} = 1/k$.

Using the disk around V4046 Sgr as a reference, with the parameters taken from (Rosenfeld, et al. 2013b) and assuming $0.1 \mu\text{m}$ dust grains and a dust-to-gas-ratio of 10^{-3} , we find a region in the upper layers of the outer disk in which photo-desorption operates more quickly than freeze-out and photo-dissociation (Fig 6). Near the disk surface photo-desorption operates more quickly than freeze-out due to the strong UV field and the low densities. In the uppermost layers photo-dissociation operates more rapidly than photo-desorption; while both processes rely on the same UV field, the decreasing number of dust grains from which CO can desorb, as well as the diminishing effects of self-shielding, lead photo-dissociation to operate more quickly than photo-desorption in the highest layers. These trends limit effective photo-desorption to a narrow layer within the disk, similar to what has been seen in more detailed chemical modeling (Öberg et al. 2015; Teague et al. 2017). The boundaries for the photo-desorption region appear to follow contours in the vertically integrated column density. Given this behavior we parameterize CO non-thermal desorption as a return to normal CO abundance in the region between $N_{\text{H}_2} = 1.3$ and $4.8 \times 10^{21} \text{ cm}^{-2}$. The CO emission is most strongly dependent on the boundary at lower column densities, corresponding to larger heights above the midplane, due to the highly optically thick nature of CO. Our choice of $N_{\text{H}_2} = 1.3 \times 10^{21} \text{ cm}^{-2}$ for photodesorption matches the boundary used in the inner disk for photodissociation of CO, ensuring that there is no discontinuity in the CO location across the freeze-out boundary. Including this parameterization for CO photo-desorption eliminates most of the residuals in the outer disk (Fig 6).

B. POSITIVE VS NEGATIVE INCLINATION

For a perfectly thin disk, there is a degeneracy between positive and negative inclinations, but protoplanetary disks have a nonzero thickness, which introduces small differences in the emission based on the sign of the inclination. In the case of the disk around HD 163296, Rosenfeld et al. (2013a) demonstrated that spatially resolving the upper and lower molecular layers of the disk indicates that the inclination is positive. While we do not resolve the layers of the disks around DM Tau, MWC 480, or V4046 Sgr, the nonzero thickness still influences the emission. Lines of sight through the half of the disk closer to the observer terminate at smaller radii, and hence warmer gas temperatures, than lines of sight through the far side of the disk. This leads to a small asymmetry in the emission from the disk that can be detected when the data are of sufficiently high S/N.

Figure 7 shows the residuals for the three systems between models with a positive and negative inclination (following the disk orientation convention outlined in Czekala et al. 2019). The disks around DM Tau and V4046 Sgr exhibit residuals that are asymmetric along the minor axis of the disk when the inclination is negative, while these residuals disappear when the inclination is positive. Conversely, the disk around MWC 480 has asymmetric residuals for a positive inclination, but more symmetric residuals for a negative disk inclinations. This is evidence that the disks around DM Tau and V4046 Sgr have positive inclinations (i.e. the north-east and north-west regions of the disk

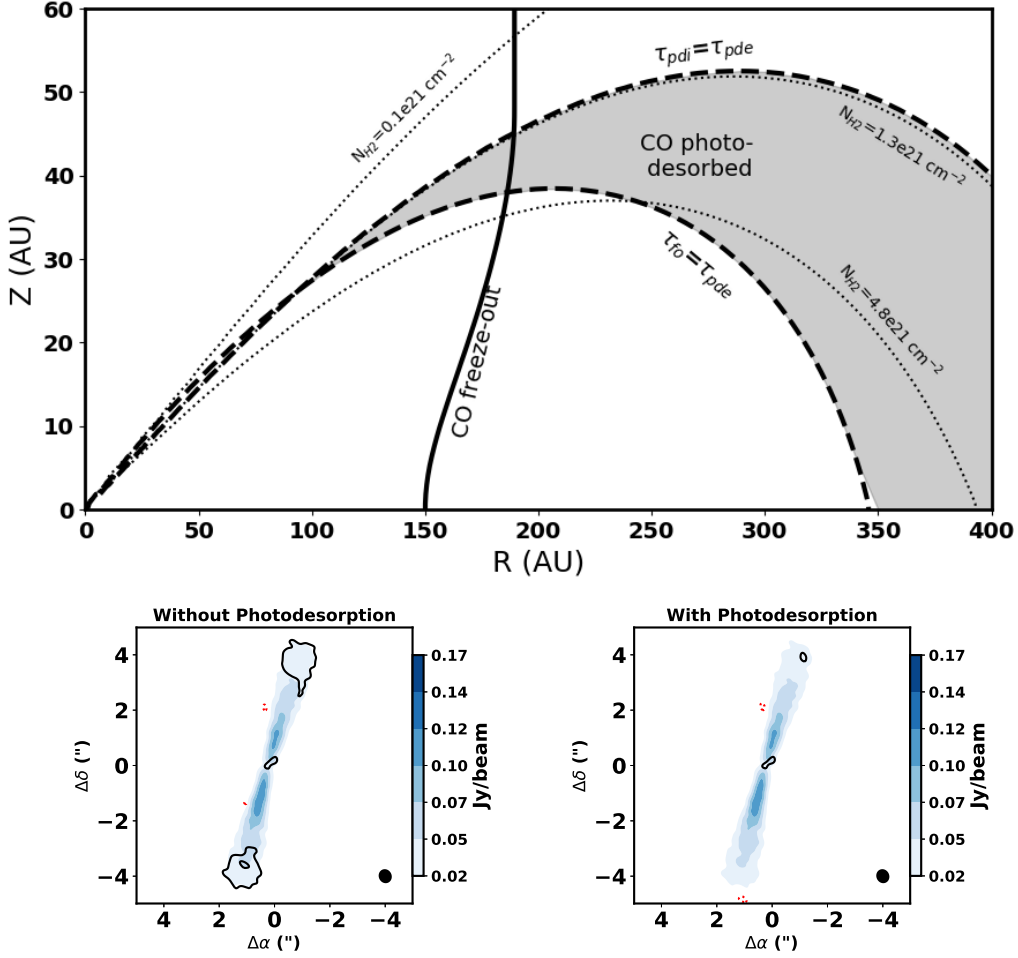


Figure 6. (*Top:*) Disk profile, indicating the boundaries between which photo-desorption can return CO from the solid phase to the gas phase. Near the midplane the freeze-out timescale is smaller than the photo-desorption timescale, due to the increase grain density and weaker radiation field, while in the surface layers photo-dissociation operates more quickly than photo-desorption, due to the limited influence of self-shielding. The boundaries where the freeze-out timescale equals the photo-desorption timescale, and where the photo-dissociation timescale is equal to the photo-desorption timescale are marked by the lower and upper dashed lines respectively. Between these two boundaries photo-desorption can return CO to the gas phase. The boundaries of this region closely follow contours of constant vertically integrated surface density (marked with dotted lines). (*Bottom:*) Residuals (black contours for data>model, red dotted contours for model>data) between the data (shown in the blue-filled contours) and a model without photodesorption (left) and including our prescription for photodesorption (right) for the central velocity channel of the CO emission from around V4046 Sgr. The addition of photodesorption accurately reproduces the majority of the emission in the outer disk that would otherwise not be included in the model.

around DM Tau and V4046 Sgr, respectively, are closer to the observer), while the disk around MWC 480 has a negative inclination (i.e. the south-west region of the disk is closer to the observer than the north-east).

C. POSTERIOR DISTRIBUTION FUNCTIONS

Here we show the two-dimensional and one-dimensional posterior distribution functions for the fiducial MCMC trials for DM Tau (Figure 8), MWC 480 (Figure 9), and V4046 Sgr (Figure 10). Figure 11 shows the chains for DM Tau trials, demonstrating that the walkers quickly converge toward a preferred solution.

REFERENCES

Akaike, H. 1974, IEEE Transactions on Automatic Control, 19, 716. Alencar, S. H. P. & Batalha, C. 2002, ApJ, 571, 378.

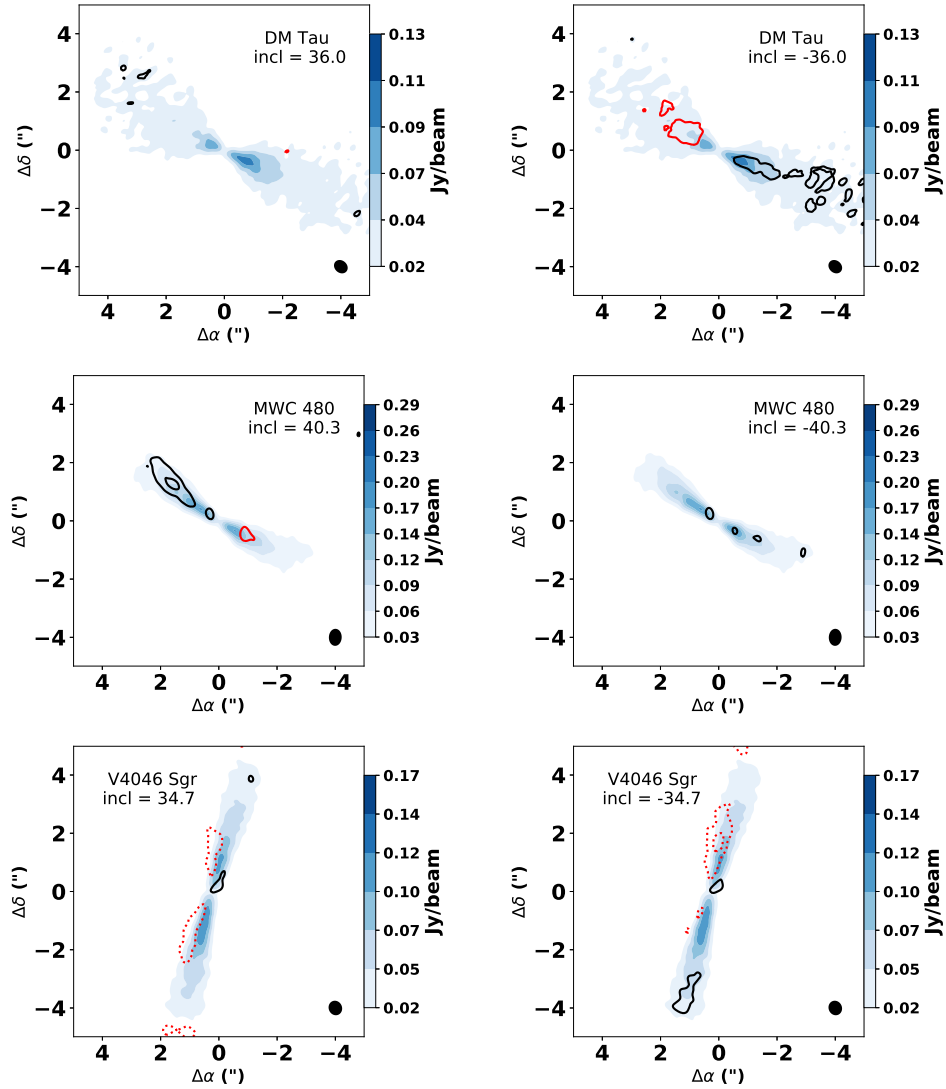


Figure 7. The nonzero thickness of the disk introduces a small asymmetry along the minor axis between a model with a positive inclination and a model with negative inclination. Given the high S/N of our data we can distinguish between these scenarios in the central velocity channel maps shown here. The residuals (black contours for data>model, red dotted contours for model>data) for negative inclinations (left column) show a clear asymmetry along the minor axis for the disks around V4046 Sgr and DM Tau but not for MWC 480. This resolves the degeneracy in the sign of the inclination, and indicates that for the disk around V4046 Sgr the north-west side is closer to the observer, for DM Tau the north-east side of the disk is closer, and for MWC 480 the south-west side of the disk is closer.

Andrews, S. M., Wilner, D. J., Espaillat, C., et al. 2011, ApJ, 732, 42.

Andrews, S. M., Rosenfeld, K. A., Kraus, A. L., et al. 2013, ApJ, 771, 129.

Ansdell, M., Williams, J. P., Trapman, L., et al. 2018, ApJ, 859, 21

Astropy Collaboration, Robitaille, T. P., Tollerud, E. J., et al. 2013, A&A, 558, A33

Bae, J., & Zhu, Z. 2018, ApJ, 859, 119.

Bai, X.-N. 2016, ApJ, 821, 80

Bai, X.-N., & Stone, J. M. 2011, ApJ, 736, 144

Bai, X.-N., & Stone, J. M. 2014, ApJ, 796, 31.

Bailer-Jones, C. A. L., Rybizki, J., Fouesneau, M., et al. 2018, AJ, 156, 58

Balbus, S. A., & Hawley, J. F. 1998, Reviews of Modern Physics, 70, 1.

Béthune, W., Lesur, G., & Ferreira, J. 2017, A&A, 600, A75.

Bergin, E. A., Cleeves, L. I., Gorti, U., et al. 2013, Nature, 493, 644.

Binks, A. S. & Jeffries, R. D. 2014, MNRAS, 438, L11.

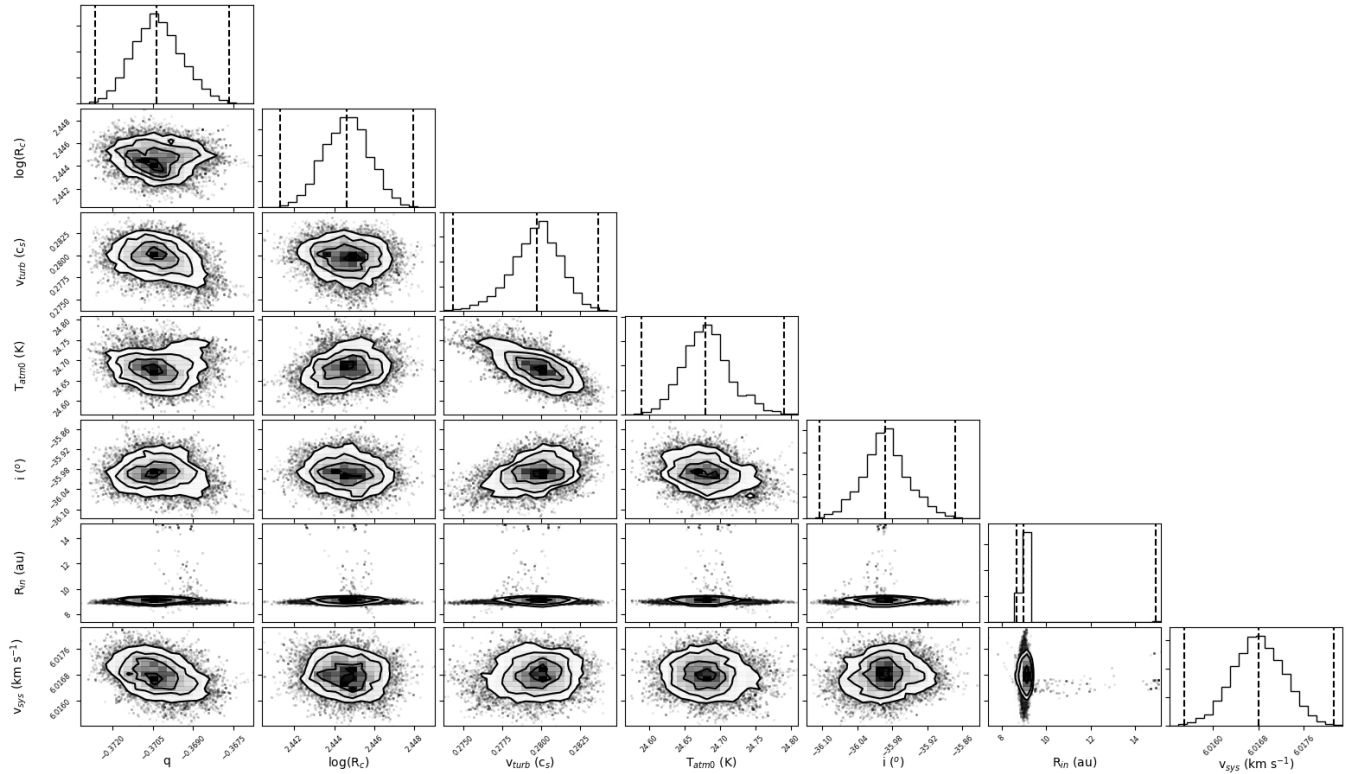


Figure 8. Corner plot showing one and two-dimensional posterior distributions for the DM Tau fiducial model. Vertical lines indicate the 1.5, 50, 99.85 percentile locations.

Birnstiel, T., Dullemond, C. P., & Brauer, F. 2010, *A&A*, 513, A79.

Boneberg, D. M., Panić, O., Haworth, T. J., et al. 2016, *MNRAS*, 461, 385.

Brickhouse, N. S., Cranmer, S. R., Dupree, A. K., et al. 2010, *ApJ*, 710, 1835.

Butler, B. 2012, *ALMA Memo*, 594, https://science.nrao.edu/facilities/alma/aboutALMA/Technology/ALMA_Memo.Series/alma594/abs594

Carr, J. S., Tokunaga, A. T. & Najita, J. 2004, *ApJ*, 603, 213.

Chen, Y.-J., Chuang, K.-J., Muñoz Caro, G. M., et al. 2014, *ApJ*, 781, 15

Ciesla, F. J. 2007, *ApJL*, 654, L159

Cleeves, L. I., Öberg, K. I., Wilner, D. J., et al. 2016, *ApJ*, 832, 110

Cleeves, L. I., Bergin, E. A., Öberg, K. I., et al. 2017, *ApJL*, 843, L3

Costigan, G., Vink, J. S., Scholz, A., et al. 2014, *MNRAS*, 440, 3444.

Cui, C., & Bai, X.-N. 2019, arXiv e-prints, arXiv:1912.02941

Curran, R. L., Argiroffi, C., Sacco, G. G., et al. 2011, *A&A*, 526, A104.

Czekala, I., Andrews, S. M., Torres, G., et al. 2016, *ApJ*, 818, 156

Czekala, I., Chiang, E., Andrews, S. M., et al. 2019, *ApJ*, 883, 22

Dartois, E., Dutrey, A., & Guilloteau, S. 2003, *A&A*, 399, 773

Donehew, B. & Brittain, S. 2011, *AJ*, 141, 46.

Dong, R., Li, S., Chiang, E., et al. 2017, *ApJ*, 843, 127.

Doppmann, G. W., Najita, J. R., Carr, J. S., et al. 2011, *ApJ*, 738, 112.

Draine, B. T. 1978, *ApJS*, 36, 595

Dullemond, C. P., Birnstiel, T., Huang, J., et al. 2018, *ApJ*, 869, L46.

Dullemond, C., Isella, A., Andrews, S., et al. 2019, arXiv e-prints, arXiv:1911.12434

Dupree, A. K., Brickhouse, N. S., Cranmer, S. R., et al. 2012, *ApJ*, 750, 73.

Dutrey, A., Guilloteau, S., & Guelin, M. 1997, *A&A*, 317, L55.

Espaillet, C., Ingleby, L., Furlan, E., et al. 2013, *ApJ*, 762, 62.

Fayolle, E. C., Bertin, M., Romanzin, C., et al. 2011, *ApJL*, 739, L36

Feigelson, E. D., Getman, K., Townsley, L., et al. 2005, *The Astrophysical Journal Supplement Series*, 160, 379.

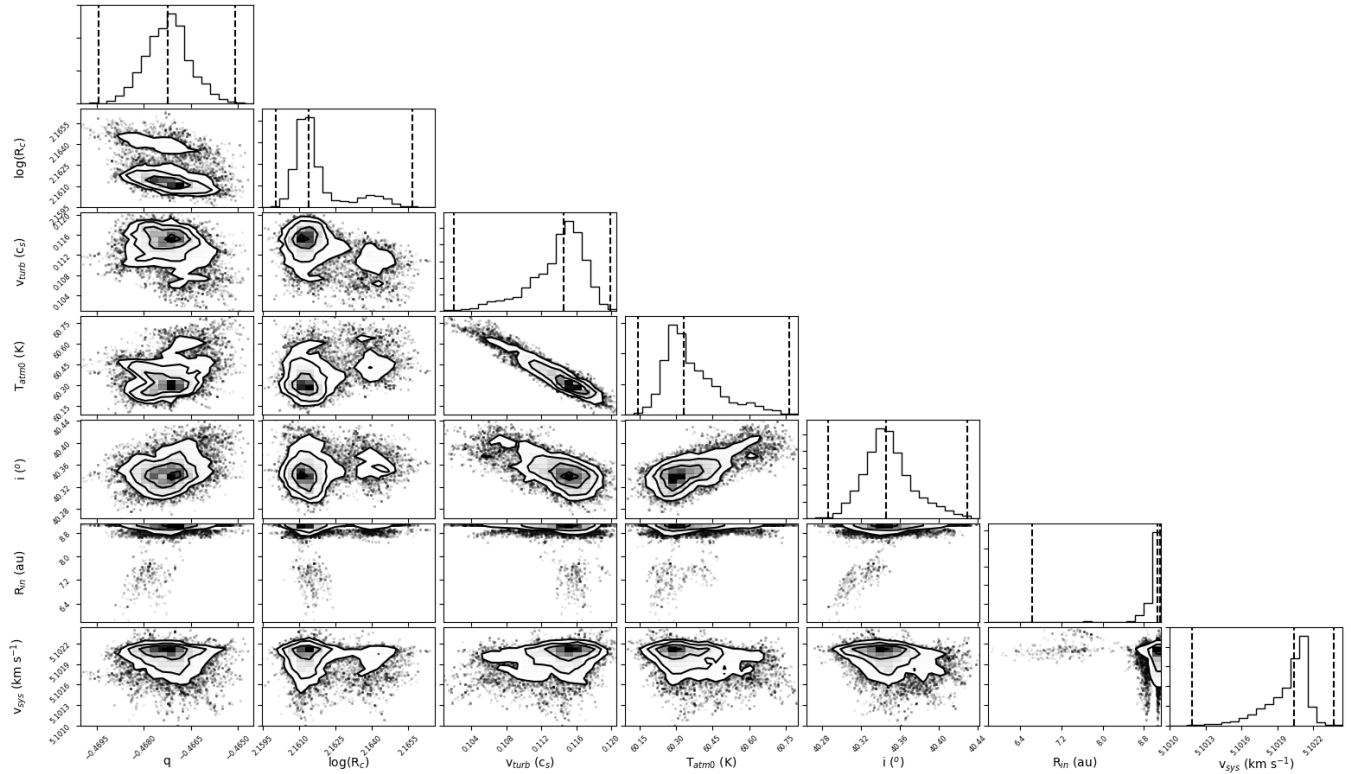


Figure 9. Corner plot showing one and two-dimensional posterior distributions for the MWC 480 fiducial model. Vertical lines indicate the 1.5, 50, 99.85 percentile locations. There is a degeneracy between T_{atm0} and v_{turb} , although it extends over a small range in parameter space.

- Fernandes, R. B., Long, Z. C., Pikhartova, M., et al. 2018, *ApJ*, 856, 103.
- Flaherty, K. M., Hughes, A. M., Rosenfeld, K. A., et al. 2015, *ApJ*, 813, 99
- Flaherty, K. M., Hughes, A. M., Rose, S. C., et al. 2017, *ApJ*, 843, 150
- Flaherty, K. M., Hughes, A. M., Teague, R., et al. 2018, *ApJ*, 856, 117.
- Flock, M., Nelson, R. P., Turner, N. J., et al. 2017, *ApJ*, 850, 131.
- Flower, D. R., Pineau Des Forêts, G., & Walmsley, C. M. 2005, *A&A*, 436, 933
- Foreman-Mackey, D., Hogg, D.W., Lang, D., & Goodman, J. 2013, *PASP*, 125, 306
- Forgan, D., Armitage, P. J., & Simon, J. B. 2012, *MNRAS*, 426, 2419.
- France, K., Schindhelm, E., Bergin, E. A., et al. 2014, *ApJ*, 784, 127.
- Fung, J., Shi, J.-M., & Chiang, E. 2014, *ApJ*, 782, 88.
- Furuya, K., & Aikawa, Y. 2014, *ApJ*, 790, 97.
- Goodman, J., & Weare, J. 2010, *Commun. Appl. Math. Comput. Sci.*, 5, 65
- Gaia Collaboration, Brown, A. G. A., Vallenari, A., et al. 2018, *A&A*, 616, A1.
- Guilloteau, S., Dutrey, A., Wakelam, V., et al. 2012, *A&A*, 548, A70.
- Guilloteau, S., Simon, M., Piétu, V., et al. 2014, *A&A*, 567, A117
- Günther, H. M. & Schmitt, J. H. M. M. 2009, *A&A*, 494, 1041.
- Habing, H. J. 1968, *BAN*, 19, 421
- Hartmann, L., Calvet, N., Gullbring, E., & D’Alessio, P. 1998, *ApJ*, 495, 385
- Henning, T., Semenov, D., Guilloteau, S., et al. 2010, *ApJ*, 714, 1511.
- Herczeg, G. J., Wood, B. E., Linsky, J. L., et al. 2004, *ApJ*, 607, 369.
- Huang, J., Öberg, K. I., & Andrews, S. M. 2016, *ApJL*, 823, L18
- Huang, J., Öberg, K. I., Qi, C., et al. 2017, *ApJ*, 835, 231.
- Huang, J., Andrews, S. M., Dullemond, C. P., et al. 2018, *ApJ*, 869, L42.
- Hughes, A. M., Wilner, D. J., Andrews, S. M., et al. 2011, *ApJ*, 727, 85.
- Ingleby, L., Calvet, N., Hernández, J., et al. 2011, *AJ*, 141, 127.
- Ingleby, L., Calvet, N., Herczeg, G., et al. 2013, *ApJ*, 767, 112.

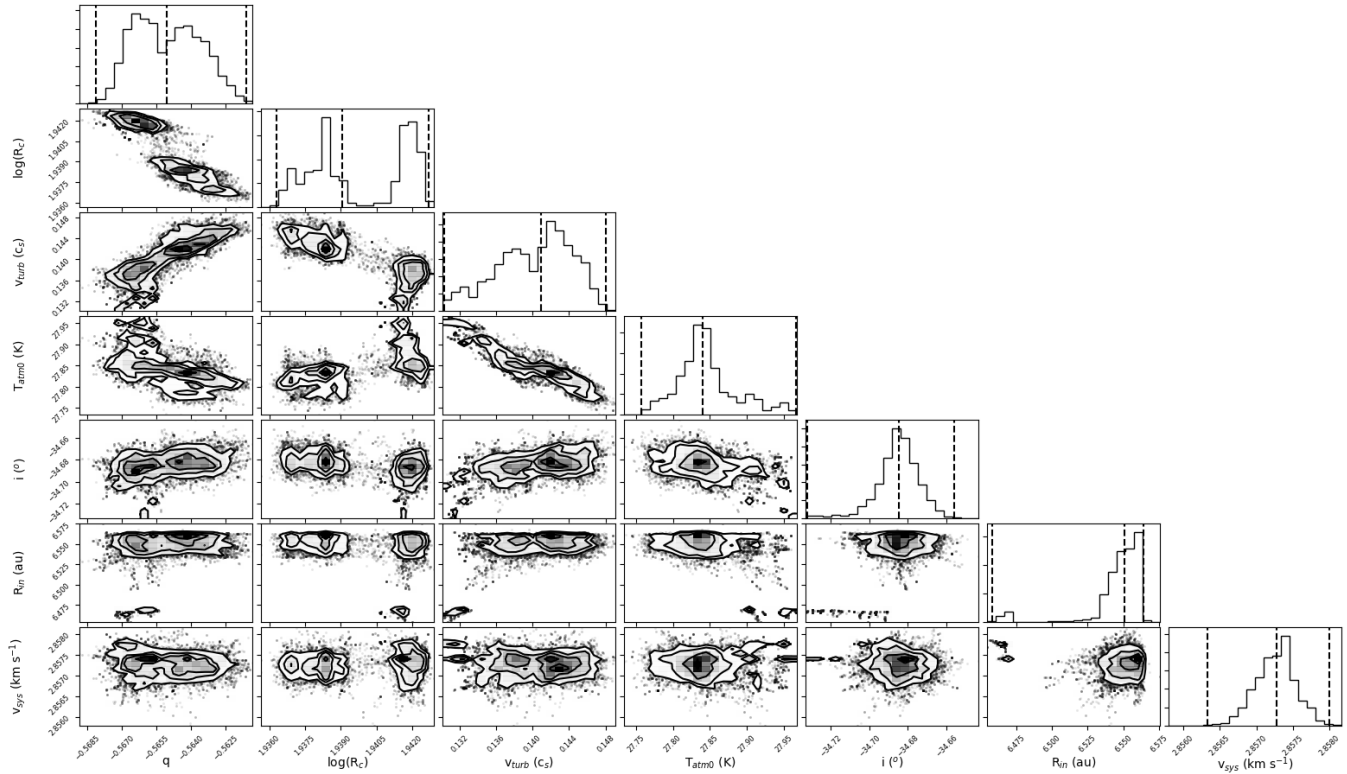


Figure 10. Corner plot showing one and two-dimensional posterior distributions for the V4046 Sgr fiducial model. Vertical lines indicate the 1.5, 50, 99.85 percentile locations. There is a degeneracy between T_{atm0} and v_{turb} , although it extends over a small range in parameter space.

Ilee, J. D., Fairlamb, J., Oudmaijer, R. D., et al. 2014, MNRAS, 445, 3723.
 Isella, A., Testi, L., Natta, A., et al. 2007, A&A, 469, 213.
 Kastner, J. H., Huenemoerder, D. P., Schulz, N. S., et al. 1999, ApJ, 525, 837.
 Kastner, J. H., Huenemoerder, D. P., Schulz, N. S., et al. 2002, ApJ, 567, 434.
 Kastner, J. H., Qi, C., Dickson-Vandervelde, D. A., et al. 2018, ApJ, 863, 106
 Klaassen, P. D., Juhász, A., Mathews, G. S., et al. 2013, A&A, 555, A73.
 Lin, M.-K., & Youdin, A. N. 2015, ApJ, 811, 17
 Lindgren, L., Hernández, J., Bombrun, A., et al. 2018, A&A, 616, A2
 Liu, S.-F., Jin, S., Li, S., et al. 2018, ApJ, 857, 87.
 Lodato, G., Scardoni, C. E., Manara, C. F., et al. 2017, MNRAS, 472, 4700.
 Loomis, R. A., Cleeves, L. I., Öberg, K. I., et al. 2015, ApJ, 809, L25.
 Luhman, K. L., Allen, P. R., Espaillat, C., et al. 2010, ApJS, 186, 111
 Lynden-Bell, D. & Pringle, J.E. 1974, MNRAS, 168, 603
 Lyra, W., & Umurhan, O. M. 2019, PASP, 131, 072001
 Mamajek, E. E. & Bell, C. P. M. 2014, MNRAS, 445, 2169.

Manara, C. F., Rosotti, G., Testi, L., et al. 2016, A&A, 591, L3.
 McClure, M. K., Bergin, E. A., Cleeves, L. I., et al. 2016, ApJ, 831, 167.
 Meeus, G., Montesinos, B., Mendigutía, I., et al. 2012, A&A, 544, A78.
 Mendigutía, I., Brittain, S., Eiroa, C., et al. 2013, ApJ, 776, 44.
 Mulders, G. D. & Dominik, C. 2012, A&A, 539, A9.
 Mulders, G. D., Pascucci, I., Manara, C. F., et al. 2017, ApJ, 847, 31.
 Najita, J. R., Doppmann, G. W., Carr, J. S., et al. 2009, ApJ, 691, 738.
 Najita, J. R., & Bergin, E. A. 2018, ApJ, 864, 168.
 Nelson, R. P., & Papaloizou, J. C. B. 2004, MNRAS, 350, 849.
 Öberg, K. I., van Dishoeck, E. F., & Linnartz, H. 2009, A&A, 496, 281
 Öberg, K. I., Qi, C., Fogel, J. K. J., et al. 2010, ApJ, 720, 480.
 Öberg, K. I., Qi, C., Wilner, D. J., et al. 2011, ApJ, 743, 152.
 Öberg, K. I., Qi, C., Fogel, J. K. J., et al. 2011, ApJ, 734, 98.

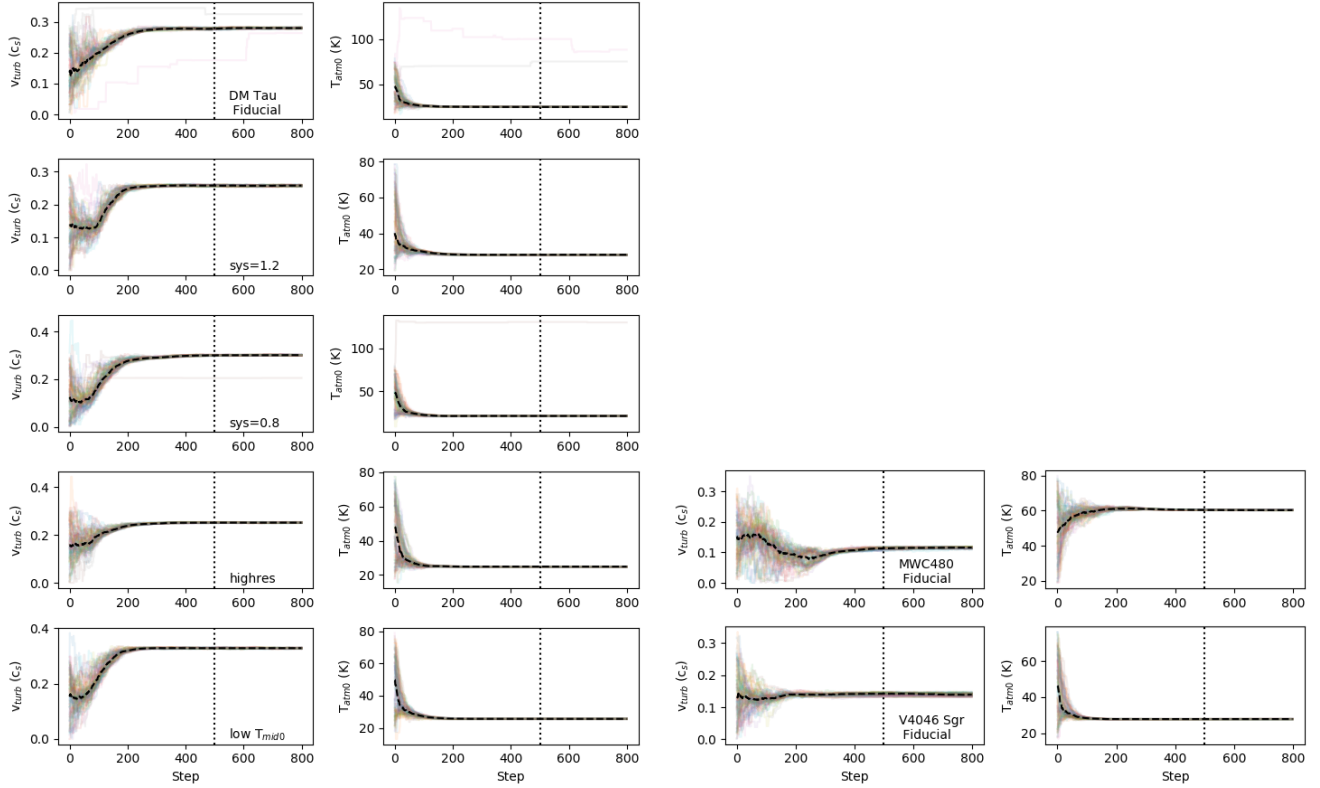


Figure 11. (Left): Progress of the walkers for the v_{turb} and T_{mid0} parameters for the DM Tau trials. Individual walkers are indicated by the light colored lines, while the median is shown by the black dashed line. The vertical dotted line divides burn-in from the region used in generating the PDFs. In each trial, the walkers quickly converge toward a preferred solution; walkers that do not converge are excluded when generating the PDFs. Note that the difference in results between the models is much larger than the statistical dispersion within a particular trial, indicating that systematic uncertainties are much larger than statistical uncertainties. (Right): Walker progressions for MWC 480 (top) and V4046 Sgr (bottom). As with DM Tau, the walkers quickly converge to a narrow range in parameter space.

Öberg, K. I., Furuya, K., Loomis, R., et al. 2015, *ApJ*, 810, 112

Ohashi, S., & Kataoka, A. 2019, *ApJ*, 886, 103

Okuzumi, S., Momose, M., Sirono, S.-i., et al. 2016, *ApJ*, 821, 82

Ormel, C. W., & Cuzzi, J. N. 2007, *A&A*, 466, 413.

Paardekooper, S.-J., Baruteau, C., & Kley, W. 2011, *MNRAS*, 410, 293.

Pascucci, I., Sterzik, M., Alexander, R. D., et al. 2011, *ApJ*, 736, 13.

Perez-Becker, D., & Chiang, E. 2011, *ApJ*, 735, 8.

Pérez, S., Casassus, S., & Benítez-Llambay, P. 2018, *MNRAS*, 480, L12.

Pérez, S., Casassus, S., Baruteau, C., et al. 2019, *AJ*, 158, 15

Piétu, V., Dutrey, A. & Guilloteau, S. 2007, *A&A*, 467, 163.

Pinte, C., Dent, W. R. F., Ménard, F., et al. 2016, *ApJ*, 816, 25.

Pinte, C., Ménard, F., Duchêne, G., et al. 2018, *A&A*, 609, A47

Pinte, C., Price, D. J., Ménard, F., et al. 2018, *ApJ*, 860, L13.

Pinte, C., van der Plas, G., Ménard, F., et al. 2019, *Nature Astronomy*, 3, 1109

Powell, D., Murray-Clay, R., Pérez, L. M., et al. 2019, *ApJ*, 878, 116

Qi, C., Öberg, K. I., & Wilner, D. J. 2013, *ApJ*, 765, 34.

Qi, C., Öberg, K. I., Espaillat, C. C., et al. 2019, *ApJ*, 882, 160

Rafikov, R. R. 2017, *ApJ*, 837, 163.

Richard, S., Nelson, R. P., & Umurhan, O. M. 2016, *MNRAS*, 456, 3571.

Riols, A., & Lesur, G. 2019, *A&A*, 625, A108

Rosenfeld, K. A., Andrews, S. M., Wilner, D. J., et al. 2012, *ApJ*, 759, 119.

Rosenfeld, K. A., Andrews, S. M., Hughes, A. M., et al. 2013, *ApJ*, 774, 16

Rosenfeld, K. A., Andrews, S. M., Wilner, D. J., et al. 2013, *ApJ*, 775, 136.

- Rosenfeld, K. A., Chiang, E., & Andrews, S. M. 2014, *ApJ*, 782, 62
- Sacco, G. G., Flaccomio, E., Pascucci, I., et al. 2012, *ApJ*, 747, 142.
- Schwarz, K. R., Bergin, E. A., Cleeves, L. I., et al. 2016, *ApJ*, 823, 91
- Schwarz, K. R., Bergin, E. A., Cleeves, L. I., et al. 2018, *ApJ*, 856, 85
- Semenov, D., & Wiebe, D. 2011, *The Astrophysical Journal Supplement Series*, 196, 25.
- Shakura, N. I., & Sunyaev, R. A. 1973, *A&A*, 24, 337
- Shi, J.-M. & Chiang, E. 2014, *ApJ*, 789, 34.
- Shi, J.-M., Zhu, Z., Stone, J. M., et al. 2016, *MNRAS*, 459, 982.
- Simon, J. B., & Armitage, P. J. 2014, *ApJ*, 784, 15.
- Simon, M., Dutrey, A. & Guilloteau, S. 2000, *ApJ*, 545, 1034.
- Simon, M. N., Pascucci, I., Edwards, S., et al. 2016, *ApJ*, 831, 169.
- Simon, M., Guilloteau, S., Beck, T. L., et al. 2019, *ApJ*, 884, 42
- Simon, J. B., Hughes, A. M., Flaherty, K. M., et al. 2015, *ApJ*, 808, 180.
- Simon, J. B., Bai, X.-N., Flaherty, K. M., et al. 2018, *ApJ*, 865, 10.
- Stepinski, T. F. 1998, *ApJ*, 507, 361.
- Suriano, S. S., Li, Z.-Y., Krasnopolsky, R., et al. 2018, *MNRAS*, 477, 1239.
- Swartz, D. A., Drake, J. J., Elsner, R. F., et al. 2005, *ApJ*, 628, 811.
- Teague, R., Semenov, D., Guilloteau, S., et al. 2015, *A&A*, 574, A137.
- Teague, R., Guilloteau, S., Semenov, D., et al. 2016, *A&A*, 592, A49.
- Teague, R., Semenov, D., Gorti, U., et al. 2017, *ApJ*, 835, 228
- Teague, R., Henning, T., Guilloteau, S., et al. 2018, *ApJ*, 864, 133.
- Teague, R., Bae, J., Bergin, E. A., et al. 2018, *ApJ*, 860, L12.
- Teague, R., Bae, J., Birnstiel, T., et al. 2018, *ApJ*, 868, 113
- Torres, C. A. O., Quast, G. R., da Silva, L., et al. 2006, *A&A*, 460, 695.
- Turner, N. J., Carballido, A., & Sano, T. 2010, *ApJ*, 708, 188
- van Boekel, R., Henning, T., Menu, J., et al. 2017, *ApJ*, 837, 132.
- Visser, R., van Dishoeck, E. F., & Black, J. H. 2009, *A&A*, 503, 323
- Vlemmings, W. H. T., Lankhaar, B., Cazzoletti, P., et al. 2019, *A&A*, 624, L7.
- Walsh, C., Daley, C., Facchini, S., et al. 2017, *A&A*, 607, A114
- Xu, R., Bai, X.-N., & Öberg, K. 2017, *ApJ*, 835, 162.
- Yang, H., Herczeg, G. J., Linsky, J. L., et al. 2012, *ApJ*, 744, 121.
- Youdin, A. N., & Lithwick, Y. 2007, *Icarus*, 192, 588.